

## Chapter 5

### Spin-orbit-coupled Bose–Einstein condensates

Yun Li<sup>1,2</sup> and Giovanni I. Martone<sup>1</sup> and Sandro Stringari<sup>1</sup>

<sup>1</sup>*Dipartimento di Fisica, Università di Trento and INO-CNR BEC Center,  
I-38123 Povo, Italy*

<sup>2</sup>*Centre for Quantum Technologies, National University of Singapore,  
3 Science Drive 2, 117542, Singapore*

The recent realization of synthetic spin-orbit coupling represents an outstanding achievement in the physics of ultracold quantum gases. In this review we explore the properties of a spin-orbit-coupled Bose–Einstein condensate with equal Rashba and Dresselhaus strengths. This system presents a rich phase diagram, which exhibits a tricritical point separating a zero-momentum phase, a spin-polarized plane-wave phase, and a stripe phase. In the stripe phase translational invariance is spontaneously broken, in analogy with supersolids. Spin-orbit coupling also strongly affects the dynamics of the system. In particular, the excitation spectrum exhibits intriguing features, including the suppression of the sound velocity, the emergence of a roton minimum in the plane-wave phase, and the appearance of a double gapless band structure in the stripe phase. Finally, we discuss a combined procedure to make the stripes visible and stable, thus allowing for a direct experimental detection.

#### 1. Introduction

A large variety of exotic phenomena in solid-state systems can take place when their constituent electrons are coupled to an external gauge field, or in the presence of strong spin-orbit coupling. For example, magnetic fields influencing the motion of the electrons are at the base of the well-known quantum Hall effect,<sup>1</sup> whereas spin-orbit coupling, i.e., the coupling between an electron's spin and its momentum, is crucial for topological insulators,<sup>2,3</sup> Majorana fermions,<sup>4</sup> spintronic devices,<sup>5</sup> etc. Ultracold atomic gases are good candidates to investigate these interesting quantum phe-

nomena. In this respect, the main difficulty arises from the fact that atoms are neutral particles, and consequently they cannot be coupled to a gauge field. In addition, they do not exhibit any coupling between their spin and their center-of-mass motion.

In the last few years there have been several proposals to realize artificial gauge fields for quantum gases, thus overcoming the problem of their neutrality.<sup>6</sup> One of these schemes relies on the notion of geometric phase,<sup>7</sup> which emerges when the motion of a particle with some internal level structure is slow enough, so that the particle follows adiabatically one of these levels. In such conditions, the particle experiences an effective vector potential. In ultracold atomic gases, several methods to implement these ideas exploit the space-dependent coupling of the atoms with a properly designed configuration of laser beams; the synthetic gauge field arises when the system follows adiabatically one of the local eigenstates of the light-atom interaction Hamiltonian (dressed states).<sup>8–11</sup> Other approaches are also possible, such as the periodic shaking of an optical lattice with special frequencies, which couples different Bloch bands.<sup>12</sup>

Since 2009, several experiments have been successful in realizing ultracold atomic gases coupled to artificial gauge fields.<sup>13–17</sup> For instance, in the experiment of Ref. 14 a space-dependent atom-light coupling was employed to simulate an effective magnetic field exerting a Lorentz-like force on neutral bosons; this procedure has been used to generate quantized vortices in Bose–Einstein condensates (BECs).

Another interesting situation occurs when the local dressed states are degenerate, giving rise to spin-orbit-coupled configurations. In particular, by using a suitable arrangement of Raman lasers, the authors of Ref. 18 managed to engineer a one-dimensional spin-orbit coupling, characterized by equal Rashba<sup>19</sup> and Dresselhaus<sup>20</sup> strengths, on a neutral atomic BEC. The same scheme has been subsequently extended to realize spin-orbit-coupled Fermi gases.<sup>21,22</sup>

These first experimental achievements have stimulated a growing interest in this field of research, resulting in a wide number of papers devoted to artificial gauge fields and, more specifically, to spin-orbit-coupled quantum gases, both from the theoretical and the experimental side. In this review we will focus on the properties of Bose–Einstein condensates with the kind of spin-orbit coupling first realized by the NIST team.<sup>18</sup> Readers who are interested in a broader overview about spin-orbit-coupled quantum gases and, more generally, about artificial gauge fields on neutral atoms, can refer to some recent reviews<sup>6,23–25</sup> and references therein.

This paper is organized as follows. In Sec. 2 we illustrate the quantum phase diagram of the system. The dynamic behavior of the gas in the two uniform phases is studied in Sec. 3. Section 4 deals with the collective excitations in the presence of harmonic trapping. Section 5 is entirely devoted to the phase exhibiting density modulations in the form of stripes: we discuss both the ground state and the excitation spectrum, and we illustrate a procedure allowing for the direct observation of the stripes. Finally, in Sec. 6 we report some brief concluding remarks.

## 2. Ground-state Phase Diagram

### 2.1. Single-particle picture

The experimental setup employed in Ref. 18 to realize spin-orbit coupling consists of a  $^{87}\text{Rb}$  Bose-Einstein condensate in the  $F = 1$  hyperfine manifold, with a bias magnetic field providing a nonlinear Zeeman splitting between the three levels of the manifold. The BEC is coupled to the field of two Raman lasers having orthogonal linear polarizations, frequencies  $\omega_L$  and  $\omega_L + \Delta\omega_L$ , and wave vector difference  $\mathbf{k}_0 = k_0\hat{\mathbf{e}}_x$ , with  $\hat{\mathbf{e}}_x$  the unit vector along the  $x$  direction. The laser field induces transitions between the three states characterized by a Rabi frequency  $\Omega$  fixed by the intensity of the lasers. This Raman process is illustrated schematically in Fig. 1. The frequency splitting  $\omega_Z$  between the states  $|F = 1, m_F = 0\rangle$  and  $|F = 1, m_F = -1\rangle$  is chosen to be very close to the frequency difference  $\Delta\omega_L$  between the two lasers, while the separation  $\omega_Z - \omega_q$  between  $|F = 1, m_F = 0\rangle$  and  $|F = 1, m_F = 1\rangle$  contains a large additional shift from Raman resonance due to the quadratic Zeeman effect. This implies that the state  $|m_F = 1\rangle$  can be neglected, and we are left with an effective spin-1/2 system, with the two spin states given by  $|\uparrow\rangle = |m_F = 0\rangle$  and  $|\downarrow\rangle = |m_F = -1\rangle$ . The single-particle Hamiltonian of this system takes the form (we set  $\hbar = m = 1$ )

$$h_0 = \frac{\mathbf{p}^2}{2} + \frac{\Omega}{2}\sigma_x \cos(2k_0x - \Delta\omega_L t) + \frac{\Omega}{2}\sigma_y \sin(2k_0x - \Delta\omega_L t) - \frac{\omega_Z}{2}\sigma_z, \quad (1)$$

where  $\sigma_k$  with  $k = x, y, z$  denotes the usual  $2 \times 2$  Pauli matrices. Hamiltonian (1) is not translationally invariant but exhibits a screwlike symmetry, being invariant with respect to helicoidal translations of the form  $e^{id(p_x - k_0\sigma_z)}$ , consisting of a combination of a rigid translation by distance  $d$  and a spin rotation by angle  $-dk_0$  around the  $z$  axis.

Let us now apply the unitary transformation  $e^{i\Theta\sigma_z/2}$ , corresponding to

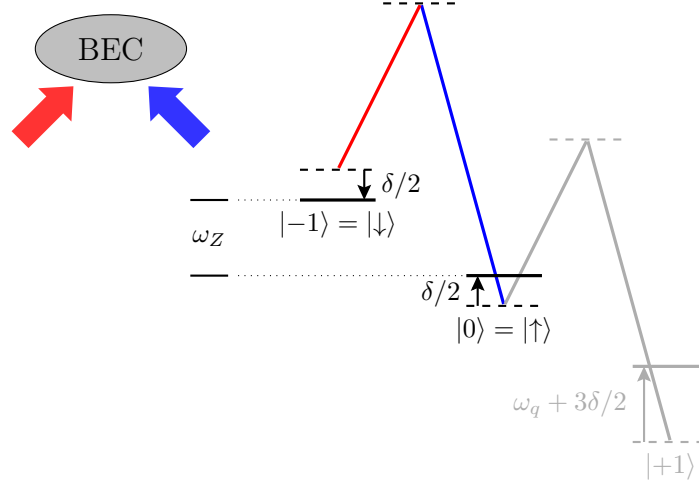


Fig. 1. Level diagram. Two Raman lasers with orthogonal linear polarizations couple the two states  $|\uparrow\rangle = |m_F = 0\rangle$  and  $|\downarrow\rangle = |m_F = -1\rangle$  of the  $F = 1$  hyperfine manifold of  $^{87}\text{Rb}$ , which differ in energy by a Zeeman splitting  $\omega_Z$ . The lasers have frequency difference  $\Delta\omega_L = \omega_Z + \delta$ , where  $\delta$  is a small detuning from the Raman resonance. The state  $|m_F = 1\rangle$  can be neglected since it has a much larger detuning, due to the quadratic Zeeman shift  $\omega_q$ .

a position and time-dependent rotation in spin space by the angle  $\Theta = 2k_0x - \Delta\omega_L t$ , to the wave function obeying the Schrödinger equation. As a consequence of the transformation, the single-particle Hamiltonian (1) is transformed into the translationally invariant and time-independent form

$$h_0^{\text{SO}} = \frac{1}{2} \left[ (p_x - k_0\sigma_z)^2 + p_\perp^2 \right] + \frac{\Omega}{2}\sigma_x + \frac{\delta}{2}\sigma_z. \quad (2)$$

The spin-orbit nature acquired by the Hamiltonian results from the non-commutation of the kinetic energy and the position-dependent rotation, while the renormalization of the effective magnetic field  $\delta = \Delta\omega_L - \omega_Z$  results from the additional time dependence exhibited by the wave function in the rotating frame. The new Hamiltonian is characterized by equal contributions of Rashba<sup>19</sup> and Dresselhaus<sup>20</sup> couplings. It has the peculiar property of violating both parity and time-reversal symmetry. It is worth pointing out that the operator  $\mathbf{p}$  entering Eq. (2) is the canonical momentum  $-i\nabla$ , with the physical velocity being given by  $\mathbf{v}_\pm = \mathbf{p} \mp k_0\hat{\mathbf{e}}_x$  for the spin-up and spin-down particles. In terms of  $\mathbf{p}$  the eigenvalues of

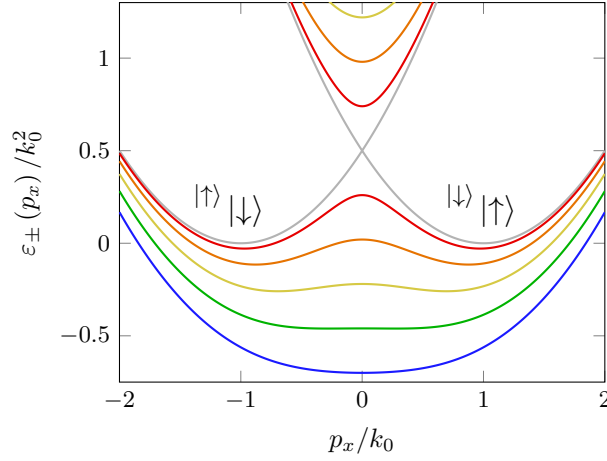


Fig. 2. Single-particle dispersion (3) at  $\delta = 0$ . Eigenenergies calculated for Raman coupling ranging from  $\Omega = 0$  (grey) to  $\Omega = 2.4 k_0^2$  (blue). The two minima in the lower branch disappear at  $\Omega = 2k_0^2$ .

Hamiltonian (2) are given by

$$\varepsilon_{\pm}(\mathbf{p}) = \frac{p_x^2 + p_{\perp}^2}{2} + E_r \pm \sqrt{\left(k_0 p_x - \frac{\delta}{2}\right)^2 + \frac{\Omega^2}{4}}, \quad (3)$$

where  $E_r = k_0^2/2$  is the recoil energy. The double-branch structure exhibited by the dispersion (3) reflects the spinor nature of the system.

We now focus on the case  $\delta = 0$  and  $\Omega \geq 0$ . In Fig. 2 we plot the dispersion (3) as a function of  $p_x$ , for different values of  $\Omega$ . The lower branch  $\varepsilon_{-}(\mathbf{p})$  exhibits, for  $\Omega < 2k_0^2$ , two degenerate minima at momenta  $\mathbf{p} = \pm k_1 \hat{\mathbf{e}}_x$  with  $k_1 = k_0 \sqrt{1 - \Omega^2/4k_0^4}$ , both capable to host Bose-Einstein condensation. At larger values of  $\Omega$  the spectrum has instead a single minimum at  $\mathbf{p} = 0$ . The effective mass of particles moving along  $x$ , fixed by the relation  $m/m^* = d^2\varepsilon/dp_x^2$ , also shows a nontrivial  $\Omega$  dependence. Near the minimum one finds

$$\frac{m}{m^*} = 1 - \left(\frac{\Omega}{2k_0^2}\right)^2 \quad \text{for } \Omega < 2k_0^2, \quad (4)$$

$$\frac{m}{m^*} = 1 - \frac{2k_0^2}{\Omega} \quad \text{for } \Omega > 2k_0^2. \quad (5)$$

Thus, the effective mass exhibits a divergent behavior at  $\Omega = 2k_0^2$ , where the double-well structure disappears and the spectrum has a  $p_x^4$  dispersion near the minimum.

Before concluding the present section, it is worth mentioning that a single-particle dispersion similar to (3) can also be achieved by trapping the atoms in a shaken optical lattice, as recently realized experimentally.<sup>17</sup> In such systems, different Bloch bands coupled through lattice shaking bear several analogies with the spin states involved in the Raman process described above.<sup>26</sup>

## 2.2. Many-body ground state

We shall now illustrate how the peculiar features of the single-particle dispersion (3) are at the origin of new interesting phases in the many-body ground state of the BEC. For a gas of  $N$  particles enclosed in a volume  $V$ , in the presence of two-body interactions, the many-body Hamiltonian takes the form

$$H = \sum_j h_0^{\text{SO}}(j) + \sum_{\sigma, \sigma'} \frac{1}{2} \int d\mathbf{r} g_{\sigma\sigma'} \rho_{\sigma}(\mathbf{r}) \rho_{\sigma'}(\mathbf{r}), \quad (6)$$

where  $h_0^{\text{SO}}$  is given by (2),  $j = 1, \dots, N$  is the particle index, and  $\sigma, \sigma'$  are the spin indices ( $\uparrow, \downarrow = \pm$ ) characterizing the two spin states. The spin-up and spin-down density operators entering Eq. (6) are defined by  $\rho_{\pm}(\mathbf{r}) = (1/2) \sum_j (1 \pm \sigma_{z,j}) \delta(\mathbf{r} - \mathbf{r}_j)$ , while  $g_{\sigma\sigma'} = 4\pi a_{\sigma\sigma'}$  are the relevant coupling constants in the different spin channels, with  $a_{\sigma\sigma'}$  the corresponding  $s$ -wave scattering lengths.

To investigate the ground state of the system we resort to the Gross-Pitaevskii mean-field approach, and we write the energy functional associated to Hamiltonian (6) as

$$E = \int d\mathbf{r} \Psi^\dagger(\mathbf{r}) h_0^{\text{SO}} \Psi(\mathbf{r}) + \int d\mathbf{r} \left[ \frac{g_{\uparrow\uparrow}}{2} |\psi_{\uparrow}(\mathbf{r})|^4 + \frac{g_{\downarrow\downarrow}}{2} |\psi_{\downarrow}(\mathbf{r})|^4 + g_{\uparrow\downarrow} |\psi_{\uparrow}(\mathbf{r})|^2 |\psi_{\downarrow}(\mathbf{r})|^2 \right], \quad (7)$$

where  $\Psi = (\psi_{\uparrow} \ \psi_{\downarrow})^T$  is the two-component condensate wave function. For simplicity, in this review we will assume  $\delta = 0$  and equal intraspecies interactions  $g_{\uparrow\uparrow} = g_{\downarrow\downarrow} \equiv g$ , unless otherwise specified; the effect of asymmetry of the coupling constants will be briefly discussed at the end of the present section. The ground-state wave function can be determined through a variational procedure based on the ansatz<sup>27</sup>

$$\Psi = \sqrt{n} \left[ C_+ \begin{pmatrix} \cos \theta \\ -\sin \theta \end{pmatrix} e^{ik_1 x} + C_- \begin{pmatrix} \sin \theta \\ -\cos \theta \end{pmatrix} e^{-ik_1 x} \right] \quad (8)$$

where  $\bar{n} = N/V$  is the average density, and  $k_1$  represents the canonical momentum where Bose-Einstein condensation takes place. For a given value of  $\bar{n}$  and  $\Omega$ , the variational parameters are  $C_+$ ,  $C_-$ ,  $k_1$  and  $\theta$ . Their values are determined by minimizing the energy (7) with the normalization constraint  $\int d\mathbf{r} \Psi^\dagger \Psi = N$ , i.e.,  $|C_+|^2 + |C_-|^2 = 1$ . Minimization with respect to  $k_1$  yields the general relation  $2\theta = \arccos(k_1/k_0)$  fixed by the single-particle Hamiltonian (2). Once the other variational parameters are determined, it is possible to calculate key physical quantities like, for example, the momentum distribution accounted for by the parameter  $k_1$ , the total density  $n(\mathbf{r}) = \Psi^\dagger \Psi$ , the longitudinal ( $s_z(\mathbf{r})$ ) and transverse ( $s_x(\mathbf{r})$ ,  $s_y(\mathbf{r})$ ) spin densities, given by

$$s_z(\mathbf{r}) = \Psi^\dagger \sigma_z \Psi = \bar{n} (|C_+|^2 - |C_-|^2) \frac{k_1}{k_0}, \quad (9)$$

$$s_x(\mathbf{r}) = \Psi^\dagger \sigma_x \Psi = -\bar{n} \left[ \frac{\sqrt{k_0^2 - k_1^2}}{k_0} + 2|C_+ C_-| \cos(2k_1 x + \phi) \right], \quad (10)$$

$$s_y(\mathbf{r}) = \Psi^\dagger \sigma_y \Psi = \bar{n} |C_+ C_-| \frac{2k_1}{k_0} \sin(2k_1 x + \phi), \quad (11)$$

with  $\phi$  the relative phase between  $C_+$  and  $C_-$ , and the corresponding spin polarizations  $\langle \sigma_k \rangle = N^{-1} \int d\mathbf{r} s_k$  with  $k = x, y, z$ . Before going on, we notice that the results (10) and (11) hold in the spin-rotated frame where the Hamiltonian takes the form (6). Since the operators  $\sigma_x$  and  $\sigma_y$  do not commute with  $\sigma_z$ , in the original laboratory frame the average value of these operators exhibits an additional oscillatory behavior analogous to the one characterizing the laser potential of Eq. (1).

The ansatz (8) exactly describes the ground state of the single-particle Hamiltonian  $h_0^{\text{SO}}$  (ideal Bose gas), reproducing all the features presented in Sec. 2.1, including the values of the canonical momentum  $k_1$ . In this case the energy is independent of  $C_\pm$ , reflecting the degeneracy of the ground state.

The same ansatz is well suited also for discussing the role of interactions, which crucially affect the explicit values of  $C_+$ ,  $C_-$  and  $k_1$ . By inserting (8) into (7), one finds that the energy per particle  $\varepsilon = E/N$  takes the form

$$\varepsilon = \frac{k_0^2}{2} - \frac{\Omega}{2k_0} \sqrt{k_0^2 - k_1^2} - F(\beta) \frac{k_1^2}{2k_0^2} + G_1 (1 + 2\beta), \quad (12)$$

where we have defined the quantities  $\beta = |C_+|^2 |C_-|^2 \in [0, 1/4]$ ,  $G_1 = \bar{n}(g + g_{\uparrow\downarrow})/4$ ,  $G_2 = \bar{n}(g - g_{\uparrow\downarrow})/4$  and the function  $F(\beta) = (k_0^2 - 2G_2) + 4(G_1 + 2G_2)\beta$ . By minimizing (12) with respect to  $\beta$  and  $k_1$  we obtain

the mean-field ground state of the system. Depending on the values of the relevant parameters  $k_0$ ,  $\Omega$ ,  $g$ ,  $g_{\uparrow\downarrow}$  and  $\bar{n}$ , the minimum can occur either at  $k_1 = 0$  or at  $k_1 \neq 0$  and  $\beta$  equal to one of the limiting values 0 and  $1/4$ . Therefore, the ground state is compatible with three distinct quantum phases; the corresponding phase diagram is shown in Fig. 3.

**(I) Stripe phase.** For small values of the Raman coupling  $\Omega$  and  $g > g_{\uparrow\downarrow}$ , the ground state is a linear combination of the two plane-wave states  $e^{\pm ik_1 x}$  with equal weights ( $|C_+| = |C_-| = 1/\sqrt{2}$ ), yielding a vanishing longitudinal spin polarization (see Eq. (9)). The most striking feature of this phase is the appearance of density modulations in the form of stripes according to the law

$$n(\mathbf{r}) = \bar{n} \left[ 1 + \frac{\Omega}{2(k_0^2 + G_1)} \cos(2k_1 x + \phi) \right]. \quad (13)$$

The periodicity of the fringes  $\pi/k_1$  is determined by the wave vector

$$k_1 = k_0 \sqrt{1 - \frac{\Omega^2}{4(k_0^2 + G_1)^2}} \quad (14)$$

and differs from the one of the laser potential, equal to  $\pi/k_0$  (see Eq. (1)). These modulations have a deeply different nature with respect to those exhibited by the density profile in the presence of usual optical lattices. Indeed, they appear as the result of a spontaneous breaking mechanism of translational invariance, with the actual position of the fringes being given by the value of the phase  $\phi$ . Because of the coexistence of BEC and crystalline order, the stripe phase shares important analogies with super-solids.<sup>28</sup> It also shares similarities with the spatial structure of smectic liquid crystals. The contrast in  $n(\mathbf{r})$  is given by

$$\frac{n_{\max} - n_{\min}}{n_{\max} + n_{\min}} = \frac{\Omega}{2(k_0^2 + G_1)} \quad (15)$$

and vanishes as  $\Omega \rightarrow 0$  as a consequence of the orthogonality of the two spin states entering Eq. (8) (in this limit  $\theta \rightarrow 0$  and  $k_1 \rightarrow k_0$ ). It is also worth mentioning that the ansatz, Eq. (8), for the stripe phase provides only a first approximation which ignores higher-order harmonics caused by the nonlinear interaction terms in the Hamiltonian.

**(II) Plane-wave phase.** For larger values of the Raman coupling, the system enters a new phase, the so-called plane-wave phase (also called the spin-polarized or de-mixed phase), where Bose-Einstein condensation takes place in a single plane-wave state with momentum  $\mathbf{p} = k_1 \hat{\mathbf{e}}_x$  ( $C_- = 0$ ), lying



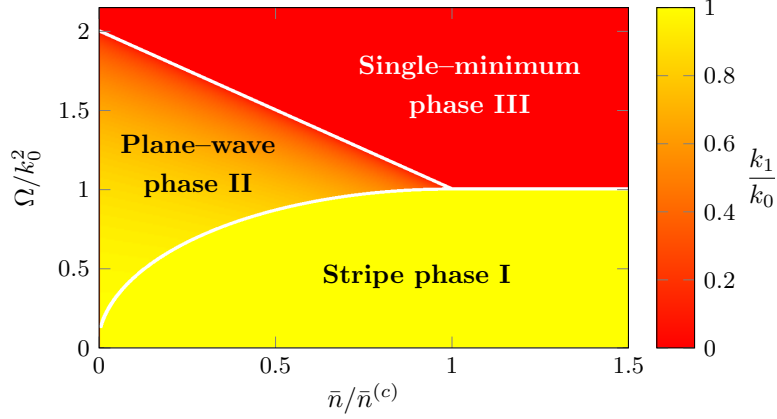


Fig. 3. Phase diagram of a spin-orbit-coupled BEC. The color represents the value of  $k_1/k_0$ . The white solid lines identify the phase transitions (I-II), (II-III) and (I-III). The diagram corresponds to a configuration with  $\gamma = (g - g_{\uparrow\downarrow})/(g + g_{\uparrow\downarrow}) = 0.0012$  consistent with the value of Ref. 18.

on the  $x$  direction (in the following we choose  $k_1 > 0$ ). In this phase, the density is uniform and the spin polarization is given by

$$\langle \sigma_z \rangle = \frac{k_1}{k_0} \quad (16)$$

with

$$k_1 = k_0 \sqrt{1 - \frac{\Omega^2}{4(k_0^2 - 2G_2)^2}}. \quad (17)$$

An energetically equivalent configuration is obtained by considering the BEC in the single-particle state with  $\mathbf{p} = -k_1 \hat{\mathbf{e}}_x$  ( $C_+ = 0$ ). The choice between the two configurations is determined by a mechanism of spontaneous symmetry breaking, typical of ferromagnetic configurations.

**(III) Single-minimum phase.** At even larger values of  $\Omega$ , the system enters the single-minimum phase (also called zero-momentum phase), where the condensate has zero momentum ( $k_1 = 0$ ), the density is uniform, and the average spin polarization  $\langle \sigma_z \rangle$  identically vanishes, while  $\langle \sigma_x \rangle = -1$ . Contrary to what one would naively expect, also the single-minimum phase exhibits nontrivial properties, as we will see in Secs. 3 and 4.

The chemical potential in the three phases can be calculated from the

energy per particle (12), and takes the form

$$\mu^{(\text{I})} = 2G_1 - \frac{k_0^2 \Omega^2}{8(k_0^2 + G_1)^2}, \quad (18)$$

$$\mu^{(\text{II})} = 2(G_1 + G_2) - \frac{k_0^2 \Omega^2}{8(k_0^2 - 2G_2)^2}, \quad (19)$$

$$\mu^{(\text{III})} = 2G_1 + \frac{k_0^2 - \Omega}{2}. \quad (20)$$

The critical values of the Rabi frequencies  $\Omega$  characterizing the phase transitions can be identified by imposing that the chemical potential (18)–(20) and the pressure  $P = n\mu(n) - \int \mu(n) dn$  be equal in the two phases at equilibrium. The transition between the stripe and the plane-wave phases has a first-order nature and is characterized by different values of the densities of the two phases. The density differences are, however, extremely small and are not visible in Fig. 3. The transition between the plane-wave and the single-minimum phases has instead a second-order nature and is characterized by a jump in the compressibility  $n^{-1}(\partial\mu/\partial n)^{-1}$  if  $G_2 \neq 0$  and by a divergent behavior of the magnetic polarizability (see Sec. 2.3). In the low density (or weak coupling) limit, i.e.,  $G_1, G_2 \ll k_0^2$ , the critical value of the Raman coupling  $\Omega^{(\text{I-II})}$  characterizing the transition between phases I and II is given by the density-independent expression<sup>27,29</sup>

$$\Omega^{(\text{I-II})} = 2k_0^2 \sqrt{\frac{2\gamma}{1+2\gamma}}, \quad (21)$$

with  $\gamma = G_2/G_1$ . The transition between phases II and III instead takes place at the higher value<sup>27</sup>

$$\Omega^{(\text{II-III})} = 2(k_0^2 - 2G_2), \quad (22)$$

provided that the condition  $\bar{n} < \bar{n}^{(c)}$  is satisfied, with  $\bar{n}^{(c)} = k_0^2/(2g\gamma)$  being the value of the density at the tricritical point shown in Fig. 3, where the three phases connect each other. For higher densities one has instead a first-order transition directly between phases I and III. We also remark that, if  $g < g_{\uparrow\downarrow}$ , only phases II and III are available, the stripe phase being always energetically unfavorable.

The previous results can be extended to the case  $\delta \neq 0$  and  $g_{\uparrow\uparrow} \neq g_{\downarrow\downarrow}$ . In general one can introduce three interaction parameters:  $G_1 = \bar{n}(g_{\uparrow\uparrow} + g_{\downarrow\downarrow} + 2g_{\uparrow\downarrow})/8$ ,  $G_2 = \bar{n}(g_{\uparrow\uparrow} + g_{\downarrow\downarrow} - 2g_{\uparrow\downarrow})/8$  and  $G_3 = \bar{n}(g_{\uparrow\uparrow} - g_{\downarrow\downarrow})/4$ . In the case of the states  $|\uparrow\rangle = |F=1, m_F=0\rangle$  and  $|\downarrow\rangle = |F=1, m_F=-1\rangle$  of  $^{87}\text{Rb}$  the values of the scattering lengths are  $a_{\uparrow\uparrow} = 101.41 a_B$  and  $a_{\downarrow\downarrow} =$

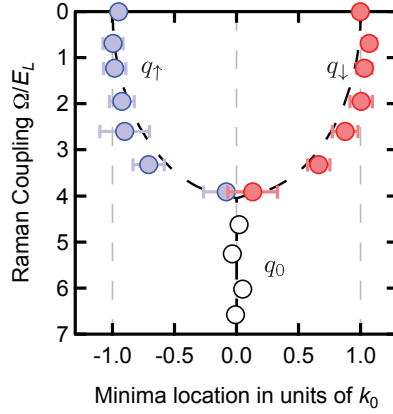


Fig. 4. Measured values of the canonical momentum versus  $\Omega$  at  $\delta = 0$ . The data points correspond to the minima of the dispersion  $\varepsilon_{-}(\mathbf{q})$  given in Eq. (3). The Raman coupling is expressed in units of the recoil energy  $E_L = k_0^2/2$ . Reprinted by permission from Macmillan Publishers Ltd: Lin *et al.*, *Nature* **471**, 83-86, © 2011.

$a_{\uparrow\downarrow} = 100.94 a_B$ , where  $a_B$  is the Bohr radius. This corresponds to  $0 < G_2 = G_3/2 \ll G_1$ . However, since the differences among the scattering lengths are very small, by properly choosing the detuning  $\delta$ , this effect can be well compensated. For example, using first order perturbation theory, one finds that the correction to the energy per particle (12) is given, in the low density (weak coupling) limit, by

$$\varepsilon^{(1)} = \left( G_3 + \frac{\delta}{2} \right) \frac{k_1}{k_0} (|C_+|^2 - |C_-|^2). \quad (23)$$

By choosing  $\delta = -2G_3$  the correction (23) vanishes, thus ensuring that the properties of the ground state of the system and the transition frequencies are not affected by the inclusion of the new terms in the Hamiltonian. If the weak coupling condition is not satisfied, the value of  $\delta$  ensuring exact compensation should depend on  $\Omega$ .

The emergence of a double minimum in the single-particle spectrum and the  $\Omega$  dependence of the value of  $k_1$  was experimentally observed by Lin *et al.* by measuring the velocity of the expanding cloud after the release of the trap<sup>18</sup> (see Fig. 4). The double-minimum structure vanishes at the predicted value (22) of the Raman coupling giving the transition between the plane-wave and the single-minimum phases. In the same experiment, at a lower value of  $\Omega$ , they identified another transition between a mixed phase, characterized by two different canonical momentum components overlap-

ping in space, and a de-mixed phase, where the two components coexist but are spatially separated. The critical Raman coupling at which the latter transition has been observed is in good agreement with the prediction  $\Omega^{(I-II)} = 0.19 E_r$  for the transition frequency between the stripe and the plane-wave phases, obtained from Eq. (21) with the  $^{87}\text{Rb}$  value  $\gamma = 0.0012$ . However, it has not been possible to observe directly the density modulations because of the smallness of their contrast and periodicity (see Sec. 5).

Finally, we mention that the critical density  $\bar{n}^{(c)}$  is very large in the experimental conditions of Ref. 18, thus preventing the access to the regime where the first-order transition between the stripe and the single-minimum phases takes place. A strong reduction of the value of  $\bar{n}^{(c)}$  could be achieved, for example, by considering configurations where the interspecies coupling strength  $g_{\uparrow\downarrow}$  is significantly smaller than the intraspecies ones  $g_{\uparrow\uparrow}$ ,  $g_{\downarrow\downarrow}$ , as discussed in Sec. 5.3.

### 2.3. Magnetic polarizability and compressibility

As already pointed out, the transition between the plane-wave and the single-minimum phases is characterized by a divergent behavior of the magnetic polarizability  $\chi_M$ . This quantity is defined as the linear response  $\chi_M = (\langle h|\sigma_z|h\rangle - \langle h=0|\sigma_z|h=0\rangle)/h$  to a static perturbation of the form  $-h\sigma_z$ , and can be calculated by generalizing the ground-state condensate wave function (8) to include the presence of a small magnetic field  $h$ . In the plane-wave and the single-minimum phases, the magnetic polarizability takes the simple form<sup>30</sup>

$$\chi_M^{(II)} = \frac{\Omega^2}{(k_0^2 - 2G_2) \left[ 4(k_0^2 - 2G_2)^2 - \Omega^2 \right]}, \quad (24)$$

$$\chi_M^{(III)} = \frac{2}{\Omega - 2(k_0^2 - 2G_2)}, \quad (25)$$

and exhibits a divergent behavior at the transition between the two phases. Indeed, when approaching the transition (22) from above or below, the values of  $\chi_M$  differ by a factor 2, revealing the second-order nature of the phase transition [31, §144]. It is worth pointing out that, if  $G_2 = 0$ , the calculation of  $\chi_M$  reduces to the ideal gas value, which is found to be related to the effective mass (4) and (5) by the simple relation

$$\frac{m^*}{m} = 1 + k_0^2 \chi_M. \quad (26)$$

The divergent behavior of the magnetic polarizability near the second-order phase transition was experimentally confirmed by Zhang *et al.* through the study of the center-of-mass oscillation<sup>32</sup> (see also the discussion in Sec. 4). Concerning the stripe phase, the calculation of  $\chi_M$  yields a complicated expression which, in the weak coupling limit  $G_1, G_2 \ll k_0^2$ , reduces to the simplified form

$$\chi_M^{(I)} = \frac{\Omega^2 - 4k_0^4}{(G_1 + 2G_2)\Omega^2 - 8G_2k_0^4}. \quad (27)$$

Notice that  $\chi_M^{(I)}$  diverges at the critical frequency providing the transition to the plane-wave phase (see Eq. (21)). However, Eq. (27) is valid only in the weak coupling limit, and the inclusion of higher-order terms makes the value of  $\chi_M$  finite at the transition.

The thermodynamic compressibility  $\kappa_T = n^{-1}(\partial\mu/\partial n)^{-1}$  in all the phases can be calculated from the expressions of the chemical potential (see Eqs. (18)–(20)),

$$1/\kappa_T^{(I)} = 2G_1 + \frac{G_1k_0^2\Omega^2}{4(k_0^2 + G_1)^3}, \quad (28)$$

$$1/\kappa_T^{(II)} = 2(G_1 + G_2) - \frac{G_2k_0^2\Omega^2}{2(k_0^2 - 2G_2)^3}, \quad (29)$$

$$1/\kappa_T^{(III)} = 2G_1. \quad (30)$$

For an interacting Bose gas, the compressibility (28)–(30) has always a finite value. It is discontinuous at the first-order transition between the stripe and the plane-wave phases; furthermore, if  $G_2 \neq 0$ , it exhibits a jump also at the second-order transition between the plane-wave and the single-minimum phases. However, as we will show in the next section, the sound velocity is continuous across the latter transition.

### 3. Dynamic Properties of the Uniform Phases

Spin-orbit coupling affects in a deep way also the dynamic behavior of a BEC, giving rise to exotic features in the excitation spectrum, such as the emergence of a rotonic structure when one approaches the transition from the plane-wave to the stripe phase,<sup>33,34</sup> the suppression of the sound velocity near the transition between the plane-wave and the single-minimum phases,<sup>34</sup> a double gapless band structure in the stripe phase,<sup>35</sup> etc. In the present section and in the next one, we focus on the dynamic behavior of

a spin-orbit-coupled BEC in the uniform phases II and III. The properties of the stripe phase will be discussed in Sec. 5.

### 3.1. Dynamic density response function. Excitation spectrum

In order to investigate the dynamic properties of a spin-orbit-coupled BEC it is useful to evaluate its dynamic density response function. This can be done by adding a time-dependent perturbation  $V_\lambda = -\lambda e^{i(\mathbf{q}\cdot\mathbf{r}-\omega t)} + \text{H.c.}$  to the single-particle Hamiltonian (2). The direction of the wave vector  $\mathbf{q}$  is characterized by the polar angle  $\alpha \in [0, \pi]$  with respect to the  $x$  axis. The density response function is then calculated through the usual definition  $\chi(\mathbf{q}, \omega) = \lim_{\lambda \rightarrow 0} \delta n_{\mathbf{q}} / (\lambda e^{-i\omega t})$ , where  $\delta n_{\mathbf{q}}$  are the fluctuations of the  $\mathbf{q}$  component of the density induced by the external perturbation.<sup>a</sup> In the following we derive  $\chi(\mathbf{q}, \omega)$  by solving the time-dependent Gross-Pitaevskii equation

$$i \frac{\partial \Psi}{\partial t} = \left[ h_0^{\text{SO}} + V_\lambda + \frac{1}{2} (g + g_{\uparrow\downarrow}) (\Psi^\dagger \Psi) + \frac{1}{2} (g - g_{\uparrow\downarrow}) (\Psi^\dagger \sigma_z \Psi) \sigma_z \right] \Psi, \quad (31)$$

where  $h_0^{\text{SO}}$  is the single-particle Hamiltonian (2) with  $\delta = 0$ . Since we are focusing on phases II and III, where the ground-state density is uniform, the spinor wave function  $\Psi$  in Eq. (31) can be written in the simple form

$$\Psi = e^{-i\mu t} \left[ \sqrt{n} \begin{pmatrix} \cos \theta \\ -\sin \theta \end{pmatrix} e^{ik_1 x} + \begin{pmatrix} u_\uparrow(\mathbf{r}) \\ u_\downarrow(\mathbf{r}) \end{pmatrix} e^{-i\omega t} + \begin{pmatrix} v_\uparrow^*(\mathbf{r}) \\ v_\downarrow^*(\mathbf{r}) \end{pmatrix} e^{i\omega t} \right]. \quad (32)$$

The terms depending on the Bogoliubov amplitudes  $u$  and  $v$  provide the deviations in the order parameter with respect to equilibrium, caused by the external perturbation. In the linear (small  $\lambda$ ) limit we find the result (near the poles one should replace  $\omega$  with  $\omega + i0$ )

$$\chi(\mathbf{q}, \omega) = \frac{-Nq^2 [\omega^2 - 4k_1 q \cos \alpha \omega + a(q, \alpha)]}{\omega^4 - 4k_1 q \cos \alpha \omega^3 + b_2(q, \alpha) \omega^2 + k_1 q \cos \alpha b_1(q, \alpha) \omega + b_0(q, \alpha)}, \quad (33)$$

where the coefficients  $a$  and  $b_i$  are even functions of  $q \equiv |\mathbf{q}|$  and  $\cos \alpha$ , implying that  $b_i(q, \alpha) = b_i(q, \pi \pm \alpha)$  (the same for  $a$ ), and their actual values depend on whether one is in phase II or III (see App. A.1). In the plane-wave phase, the odd terms in  $\omega$  entering the response function reflect the lack of parity and time-reversal symmetry of the ground-state wave

<sup>a</sup>The spin-density response function can be calculated with an analogous procedure by adding a perturbation  $\sigma_z V_\lambda$  to (2).

function; in the single-minimum phase, however, one has  $k_1 = 0$  and thus the symmetry is restored.

Notice that the response function (33) reduces to the usual Bogoliubov form  $\chi(\mathbf{q}, \omega) = -Nq^2/[\omega^2 - q^2(2G_1 + q^2/4)]$  when  $G_2 = 0$  and  $\Omega = 0$ , characterizing the response of a BEC gas in the absence of spin-orbit coupling. It is also worth pointing out that, since  $V_\lambda$  commutes with the unitary transformation yielding the Hamiltonian in the spin-rotated frame (see Sec. 2.1), the expression for  $\chi(\mathbf{q}, \omega)$  is the same as in the original laboratory frame, and thus all the results based on the calculation in the spin-rotated frame are relevant for actual experiments.

The frequencies of the elementary excitations are given by the poles of the response function  $\chi$ , i.e., by the zeros of

$$\omega^4 - 4k_1q \cos \alpha \omega^3 + b_2 \omega^2 + k_1q \cos \alpha b_1 \omega + b_0 = 0. \quad (34)$$

The solutions of this equation provide two separated branches, as shown in Fig. 5(a) and (b) for phase II and phase III respectively. The lower one is gapless and exhibits a phonon dispersion at small  $q$ , while the upper one is gapped as a consequence of the Raman coupling. For example, in phase III the gap between the two branches is given, at  $\mathbf{q} = 0$ , by  $\Delta = \sqrt{\Omega(\Omega + 4G_2)}$ . Differently from the single-minimum phase, the excitation spectrum in the plane-wave phase is not symmetric under inversion of  $q_x$  into  $-q_x$ , as a consequence of the symmetry-breaking terms appearing in Eq. (33). For negative values of  $q_x$ , the lower branch in phase II exhibits a very peculiar feature, resulting in the emergence of a roton minimum, which becomes more and more pronounced as one approaches the transition to the stripe phase. The occurrence of the rotonic structure in spin-orbit-coupled BECs shares interesting analogies with the case of dipolar gases in quasi-2D configurations<sup>36</sup> and of condensates with soft-core, finite-range interactions.<sup>37,38</sup> The physical origin of the roton minimum is quite clear. In phase II the ground state is twofold degenerate, and it is very favorable for atoms to be transferred from the BEC state with momentum  $\mathbf{p} = k_1\hat{\mathbf{e}}_x$  to the empty state at  $\mathbf{p} = -k_1\hat{\mathbf{e}}_x$ . The excitation spectrum has been recently measured using Bragg spectroscopy techniques, confirming the occurrence of a characteristic rotonic structure<sup>39,40</sup> (see also Ref. 41 for the case of shaken optical lattices).<sup>b</sup>

<sup>b</sup>In the experiments of Refs. 39–41 the excitation spectrum has been measured on top of the BEC state with momentum  $\mathbf{p} = -k_1\hat{\mathbf{e}}_x$ , for which the roton minimum, differently from the case discussed above, appears at positive values of  $q_x$ .

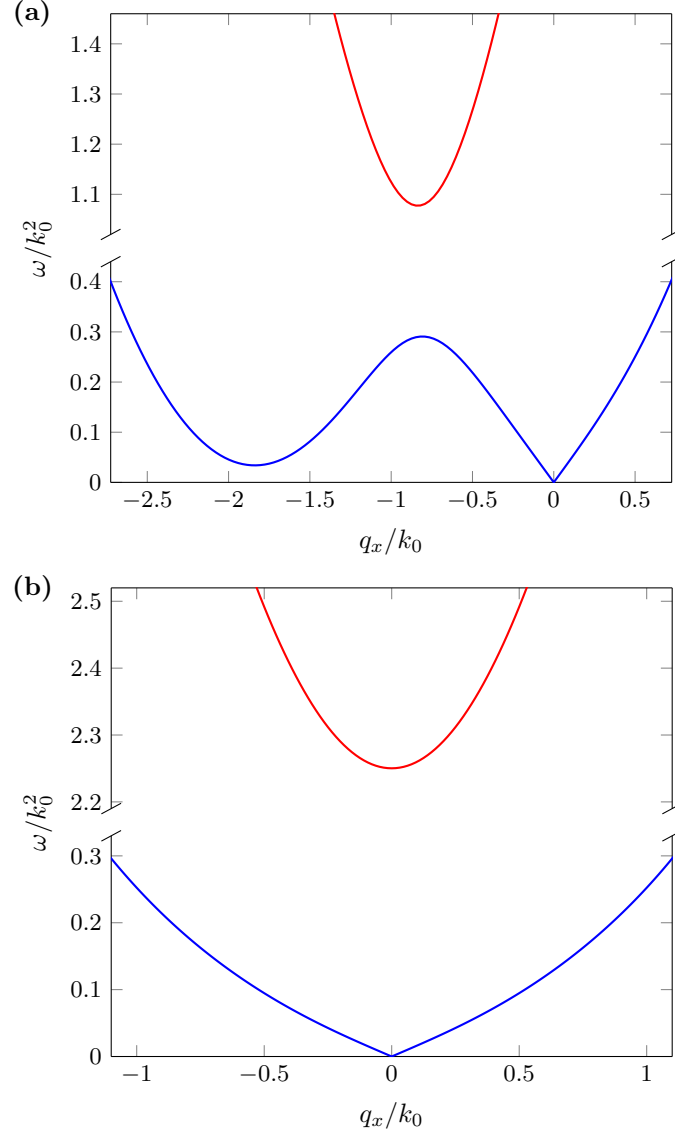


Fig. 5. Excitation spectrum **(a)** in phase II ( $\Omega/k_0^2 = 0.85$ ) and **(b)** in phase III ( $\Omega/k_0^2 = 2.25$ ) as a function of  $q_x$  ( $q_y = q_z = 0$ ), calculated in the experimental conditions of Ref. 32. The blue and red lines represent the lower and upper branches, respectively. In phase II the spectrum is not symmetric and exhibits a roton minimum for negative  $q_x$ , whose energy becomes smaller and smaller as one approaches the transition to the stripe phase at  $\Omega/k_0^2 = 0.095$ . The other parameters:  $G_1/k_0^2 = 0.12$ ,  $\gamma = G_2/G_1 = 10^{-3}$ .



### 3.2. Static response function and static structure factor

The static response function  $\chi(\mathbf{q}) \equiv \chi(\mathbf{q}, \omega = 0)/N$  can be derived directly from Eq. (33). Its  $q = 0$  value  $\mathcal{K} \equiv \chi(q = 0)$  is given by

$$\mathcal{K}_{\text{II}}^{-1} = 2G_1 + \frac{2G_2 k_1^2 (k_1^2 \cos^2 \alpha + k_0^2 \sin^2 \alpha - 2G_2)}{k_1^2 (k_0^2 \cos^2 \alpha - 2G_2) + k_0^4 \sin^2 \alpha}, \quad (35)$$

$$\mathcal{K}_{\text{III}}^{-1} = 2G_1 \quad (36)$$

in the plane-wave phase II and the single-minimum phase III, respectively. The anisotropy of  $\mathcal{K}$  in phase II caused by the spin interaction term  $G_2$  is revealed by the last term of Eq. (35) which depends on the polar angle  $\alpha$ . It is also worth pointing out that  $\mathcal{K}_{\text{II}}$  coincides with the thermodynamic compressibility  $\kappa_T^{(\text{II})}$  (see Eq. (29)) only along the  $x$  direction, i.e., when  $\sin \alpha = 0$ . In this case,  $\mathcal{K}$  also exhibits a jump at the transition between phases II and III. This marks a difference with respect to the behavior of the frequencies of the elementary excitations, fixed by Eq. (34), which are always continuous functions of  $\Omega$  at the transition for all values of  $\mathbf{q}$ .

Far from the phonon regime, the occurrence of the roton minimum is reflected in an enhancement in the static response function  $\chi(q_x)$  close to the roton momentum, as shown in Fig. 6, representing a typical tendency of the system towards crystallization. When the roton frequency vanishes,  $\chi(q_x)$  exhibits a divergent behavior. A simple analytic expression for the corresponding value of the Raman coupling  $\Omega$  is obtained in the weak coupling limit  $G_1, G_2 \ll k_0^2$ , where we find that the critical value exactly coincides with the value (see Eq. (21)) characterizing the transition between the plane-wave and the stripe phases. For larger values of the coupling constants  $G_1$  and  $G_2$ , the critical value takes place for values of the Raman coupling smaller than the value at the transition, exhibiting the typical spinoidal behavior of first-order liquid-crystal phase transitions.

The dynamic structure factor at  $T = 0$  can be calculated from the response function (33) through the relation  $S(\mathbf{q}, \omega) = \pi^{-1} \text{Im} \chi(\mathbf{q}, \omega)$  for  $\omega \geq 0$  and  $S(\mathbf{q}, \omega) = 0$  for negative  $\omega$ . In the plane-wave phase, the condition  $\text{Im} \chi(\mathbf{q}, \omega) = -\text{Im} \chi(-\mathbf{q}, -\omega)$ , characterizing the imaginary part of the response function, is still satisfied, but the symmetry relation  $\text{Im} \chi(\mathbf{q}, \omega) = \text{Im} \chi(-\mathbf{q}, \omega)$  is not ensured, and consequently one finds  $S(\mathbf{q}, \omega) \neq S(-\mathbf{q}, \omega)$ . This affects several well-known equalities involving sum rules, which have to be formulated in a more general way to account for the breaking of inversion symmetry in the plane-wave phase. An example is the  $f$ -sum rule  $\int d\omega [S(\mathbf{q}, \omega) + S(-\mathbf{q}, \omega)] \omega = Nq^2$ , which is exactly

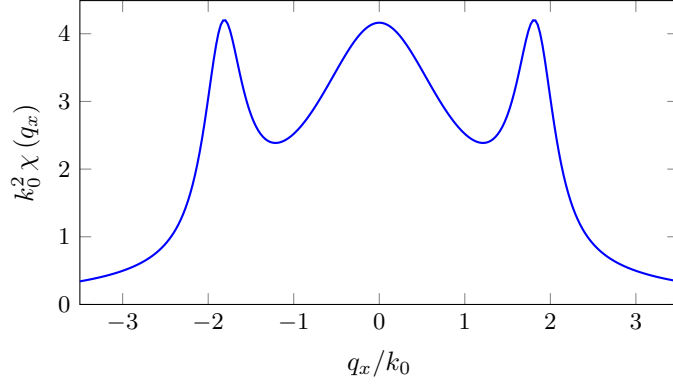


Fig. 6. Static response in phase II as a function of  $q_x$  ( $q_y = q_z = 0$ ). The curve is symmetric and exhibits a typical peak near the roton momentum. The parameters are  $\Omega/k_0^2 = 0.85$ ,  $G_1/k_0^2 = 0.12$  and  $\gamma = G_2/G_1 = 10^{-3}$ .

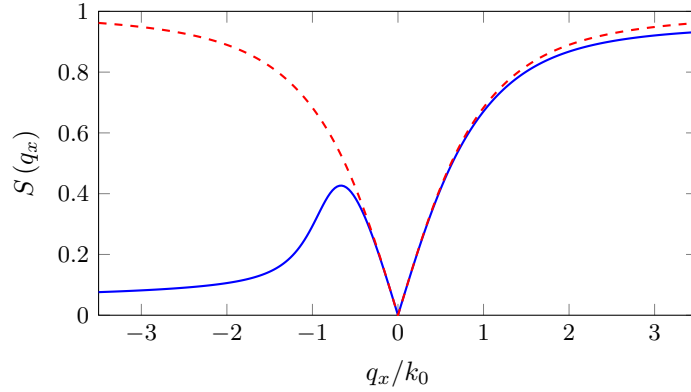


Fig. 7. Contribution of the lower branch to the static structure factor in phase II as a function of  $q_x$  (blue solid line), compared with the total  $S(q_x)$  (red dashed line). The parameters are  $\Omega/k_0^2 = 0.85$ ,  $G_1/k_0^2 = 0.12$  and  $\gamma = G_2/G_1 = 10^{-3}$ .

satisfied, as one can deduce from the correct large  $\omega$  behavior of the density response function:  $\chi(\mathbf{q}, \omega)_{\omega \rightarrow \infty} = -Nq^2/\omega^2$ .<sup>42</sup> On the other hand, the inversion symmetry of the static structure factor  $S(\mathbf{q}) = \int_0^\infty d\omega S(\mathbf{q}, \omega)/N$  is always ensured, since it is a general feature following from the completeness relation and the commutation relation involving the density operators:  $S(\mathbf{q}) - S(-\mathbf{q}) = \langle [\rho_{\mathbf{q}}, \rho_{-\mathbf{q}}] \rangle = 0$ .

It is worth pointing out that, despite the strong enhancement exhibited

by the static response function  $\chi(q_x)$ , the static structure factor  $S(q_x)$  does not exhibit any peaked structure near the roton point. This is different from what happens, for example, in superfluid helium.<sup>c</sup> In Fig. 7 we show the static structure factor  $S(q_x)$  together with the contribution to the integral  $S(q_x) = \int d\omega S(q_x, \omega)/N$  arising from the lower branch of the elementary excitations. The figure shows that the lower-branch contribution is not symmetric for exchange of  $q_x$  into  $-q_x$ , even if the total  $S(q_x)$  is symmetric, as we have showed previously. Remarkably, the strength carried by the lower branch is significantly peaked for intermediate values of  $q_x$  between the phonon and the roton regimes, in the so-called maxon region, where the lower branch of the excitation spectrum exhibits a maximum.

### 3.3. Velocity and density vs spin nature of the sound mode

The low-frequency excitations at small  $q$ , i.e., the sound waves, can be easily obtained by setting  $\omega = cq$ , where  $c$  is the sound velocity, and keeping the leading terms proportional to  $q^2$  in Eq. (34). This allows us to obtain the sound velocity in the plane-wave and the single-minimum phases,

$$c_{II} = \frac{1}{k_0^4 - 2G_2k_1^2} \left\{ G_2k_1 (k_0^2 - k_1^2) \cos \alpha + \sqrt{2 [G_1k_0^4 + G_2k_1^2 (k_0^2 - 2G_1 - 2G_2)] [k_0^4 - 2G_2k_1^2 - k_0^2 (k_0^2 - k_1^2) \cos^2 \alpha]} \right\}, \quad (37)$$

$$c_{III} = \sqrt{2G_1 \left( 1 - \frac{2k_0^2 \cos^2 \alpha}{\Omega + 4G_2} \right)}. \quad (38)$$

Approaching the transition between the two phases, both sound velocities exhibit a strong reduction along the  $x$  direction ( $\cos \alpha = \pm 1$ ), caused by the spin-orbit coupling. This suppression can be understood in terms of the increase of the effective mass associated with the single-particle dispersion (3). At the transition, where the velocity of sound modes propagating along the  $x$  direction vanishes, the elementary excitations exhibit a different  $q^2$  dependence. On the other hand, the sound velocities along the other directions ( $\alpha \neq 0, \alpha \neq \pi$ ) remain finite at the transition. The sound velocity in phase II shows a further interesting feature caused by the lack

<sup>c</sup>At finite temperature  $T$  one instead expects the static structure factor to be significantly peaked near the roton minimum, provided the roton energy is small compared to  $T$ , as a consequence of the thermal excitations of rotons, similarly to what is predicted for quasi-2D dipolar gases.<sup>43</sup>

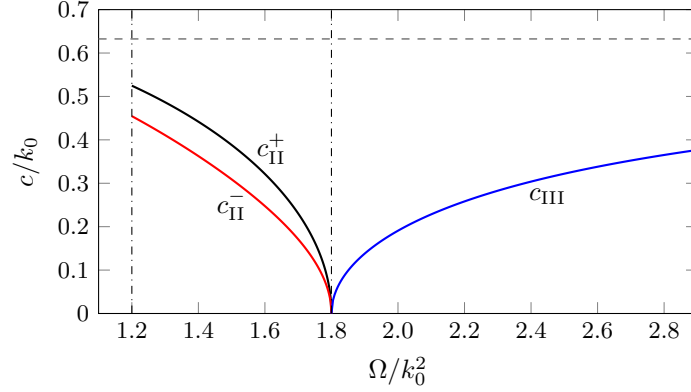


Fig. 8. Sound velocity as a function of the Raman coupling for the following choice of parameters:  $G_1/k_0^2 = 0.2$ ,  $G_2/k_0^2 = 0.05$ . The two sound velocities in phase II correspond to phonons propagating in the direction parallel ( $c_{II}^+$ ) and antiparallel ( $c_{II}^-$ ) to  $k_1$ . The horizontal dashed line corresponds to the value  $\sqrt{2G_1} = 0.63 k_0$  of the sound velocity in the absence of spin-orbit and Raman coupling. The vertical dash-dotted lines indicate the critical values of  $\Omega$  at which the I-II and II-III phase transitions take place.

of parity symmetry. The asymmetry effect in  $c_{II}$  is due to the presence of the first term in the numerator of Eq. (37), therefore the symmetry will be recovered if  $G_2 = 0$  or  $\alpha = \pi/2$  (corresponding to phonons propagating along the directions orthogonal to the  $x$  axis).

The role played by the spin degree of freedom in the propagation of the sound can be better understood by relating the sound velocity to the magnetic polarizability  $\chi_M$  (see Eqs. (24) and (25)) and the  $q = 0$  static response  $\mathcal{K}$  (see Eqs. (35) and (36)). One finds the result

$$c(\alpha)c(\alpha + \pi) = \frac{1 + k_0^2 \chi_M \sin^2 \alpha}{\mathcal{K} (1 + k_0^2 \chi_M)}, \quad (39)$$

holding in both phases II and III. The above equation generalizes the usual relation  $c^2 = 1/\mathcal{K} = n(\partial\mu/\partial n)$  between the sound velocity and the compressibility holding in usual superfluids. It explicitly shows that, along the  $x$  direction, where  $\sin \alpha = 0$ , the sound velocity  $c$  vanishes at the transition because of the divergent behavior of the magnetic polarizability. The sound velocity along the  $x$  axis as a function of  $\Omega$  is shown in Fig. 8 for a configuration with relatively large  $G_2$ , emphasizing the difference between  $c_{II}^+ = c_{II}(\alpha = 0)$  and  $c_{II}^- = c_{II}(\alpha = \pi)$ . The suppression effect exhibited by the sound velocity near the II-III phase transition is particularly remarkable in the single-minimum phase III where BEC takes place in the  $\mathbf{p} = 0$

state and the compressibility of the gas is unaffected by spin-orbit coupling. It explicitly reveals the mixed density and spin nature of the sound waves, with the spin nature becoming more and more important as one approaches the phase transition where  $\chi_M$  diverges.

The combined density and spin nature of sound waves is also nicely revealed by the relative amplitudes of the density  $\delta n$  and spin-density  $\delta s$  oscillations in the  $q \rightarrow 0$  limit, characterizing the propagation of sound. In terms of the magnetic polarizability  $\chi_M$  we find

$$\left(\frac{\delta s}{\delta n}\right)_{\text{II}} = \frac{\sqrt{1 + (k_0^2 - 2G_2)\chi_M}}{1 + k_0^2\chi_M} + \frac{k_0\chi_M\cos\alpha}{1 + k_0^2\chi_M} \sqrt{\frac{2[G_2 + G_1(1 + k_0^2\chi_M)]}{1 + k_0^2\chi_M\sin^2\alpha}}, \quad (40)$$

$$\left(\frac{\delta s}{\delta n}\right)_{\text{III}} = \frac{2k_0\chi_M\cos\alpha\sqrt{G_1}}{\sqrt{2(1 + k_0^2\chi_M)(1 + k_0^2\chi_M\sin^2\alpha)}} \quad (41)$$

in the plane-wave and the single-minimum phases respectively. The above equations show that, near the transition between phases II and III, the amplitude of the spin-density fluctuations  $\delta s$  of the sound waves propagating along the  $x$  direction ( $\sin\alpha = 0$ ) is strongly enhanced with respect to the density fluctuations  $\delta n$ , as a consequence of the divergent behavior of the magnetic polarizability. In particular, very close to the phase transition the relative amplitude is given by

$$\frac{\delta s}{\delta n} \sim \sqrt{2G_1\chi_M} \quad (42)$$

in both phases II and III. This suggests that an effective way to excite these phonon modes near the transition is through a coupling with the spin degree of freedom as recently achieved in two-photon Bragg experiments on Fermi gases.<sup>44</sup> For sound waves propagating in the direction orthogonal to  $x$  the situation is instead different. In particular in phase III sound waves are purely density oscillations ( $\delta s = 0$ ).

It is finally interesting to understand the role played by the sound waves in terms of sum rules. The phonon mode exhausts the compressibility sum rule  $\int d\omega [S(\mathbf{q}, \omega) + S(-\mathbf{q}, \omega)]/\omega$  at small  $q$ , as one can easily prove from Eq. (33). However, different from ordinary superfluid, it gives only a small contribution to the  $f$ -sum rule as one approaches the second-order transition. This contribution becomes vanishingly small at the transition for wave vectors  $\mathbf{q}$  oriented along the  $x$  direction. Also, the static structure factor  $S(\mathbf{q})$  is strongly quenched compared to usual BECs. This results in

an enhancement of the quantum fluctuations of the order parameter, as predicted by the uncertainty principle inequality.<sup>45,46</sup> This effect is, however, small because the sound velocity vanishes only along the  $x$  direction.<sup>27</sup>

#### 4. Collective Excitations in the Trap

In this section we discuss the collective excitations for a harmonically trapped BEC with spin-orbit coupling. First one should notice that, in typical experimental conditions, the spin-orbit coupling strength, usually quantified by the recoil energy  $E_r = k_0^2/2$ , is much larger than the trapping frequencies. As a consequence, one expects that the three phases occurring in uniform matter due to the spin-orbit coupling survive also in the presence of harmonic trapping. This can be verified by solving numerically the Gross–Pitaevskii equation

$$i\frac{\partial\Psi}{\partial t} = \left[ h_0^{\text{SO}} + V_{\text{ext}}(\mathbf{r}) + \frac{1}{2}(g + g_{\uparrow\downarrow})(\Psi^\dagger\Psi) + \frac{1}{2}(g - g_{\uparrow\downarrow})(\Psi^\dagger\sigma_z\Psi)\sigma_z \right] \Psi \quad (43)$$

for the condensate wave function, with  $V_{\text{ext}}(\mathbf{r}) = (\omega_x^2 x^2 + \omega_y^2 y^2 + \omega_z^2 z^2)/2$  representing the external trapping potential. Figure 9 gives an example of the momentum distribution and the spin polarization of a trapped spin-orbit-coupled BEC as a function of the Raman coupling. For simplicity, we have considered harmonic trapping only along the  $x$  direction. One can see that the three phases discussed in the bulk case show up also here. It is worth mentioning that in the low density limit, where the interaction energy is much smaller than the recoil energy, the value of  $\Omega/k_0^2$  at the transitions (21) and (22) is almost density-independent, therefore even in the presence of a trap they can be well identified using the results obtained in the bulk.

##### 4.1. Dipole mode: a sum-rule approach

Among the various excitations exhibited by a trapped spin-orbit-coupled gas, the dipole mode deserves a special attention. It corresponds to the oscillation of the center-of-mass of the system, and can be easily excited experimentally.<sup>47</sup> For a conventional trapped gas without spin-orbit coupling, the oscillation along a certain direction, for example the  $x$  axis, is excited by the dipole operator  $X = \sum_j x_j$ , and its frequency is equal to the frequency  $\omega_x$  of the harmonic trap. In the presence of spin-orbit coupling, the behavior of the dipole oscillation can be studied using the formalism of

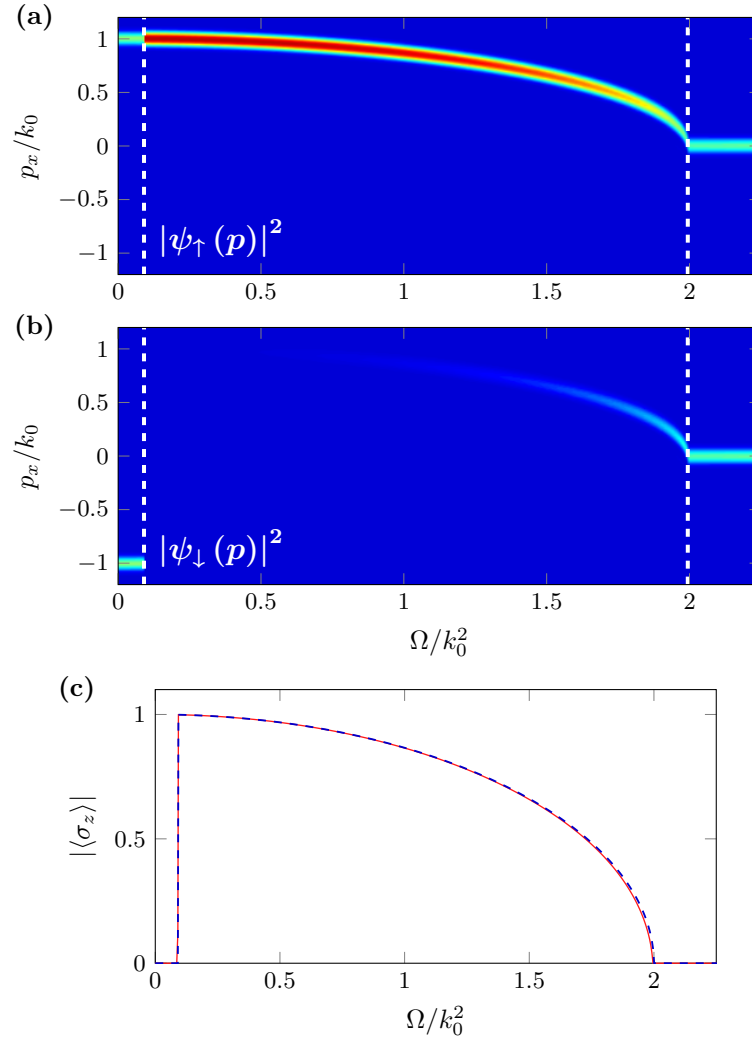


Fig. 9. **(a-b)**. Momentum distribution for the two spin components as a function of  $\Omega$ . The white dashed lines indicate the transition frequencies calculated using (21) and (22). **(c)**. Spin polarization  $|\langle \sigma_z \rangle| = |N_{\uparrow} - N_{\downarrow}|/N$  as a function of  $\Omega$  in the trapped case (red solid line) and in the uniform case using the density in the center of the trap (blue dashed line). The parameters are chosen as follows:  $\omega_x = 2\pi \times 40$  Hz,  $\omega_x/k_0^2 = 0.01$ ,  $\delta = 0$ ,  $g_{\uparrow\uparrow} = g_{\downarrow\downarrow} = 4\pi \times 101.20 a_B$ ,  $g_{\uparrow\downarrow} = 4\pi \times 100.94 a_B$ , where  $a_B$  is the Bohr radius. The density in the center of the trap corresponds to  $n \simeq 1.9 \times 10^{13} \text{ cm}^{-3}$ .

sum rules.<sup>30</sup> A major advantage of this method is that it can reduce the calculation of the dynamical properties of the many-body system to the knowledge of a few key parameters relative to the ground state.

The starting point of our analysis is represented by the definition of the  $k$ -th moment of the dynamic structure factor for a general operator  $F$ , given at zero temperature by<sup>d</sup>

$$m_k(F) = \sum_n (E_n - E_0)^k |\langle 0|F|n\rangle|^2. \quad (44)$$

Here  $|0\rangle$  and  $|n\rangle$  are, respectively, the ground state and the  $n$ -th excited state of the many-body Hamiltonian (6), now including the external trapping potential in the single-particle contributions

$$h_0^{\text{SO}}(j) = \frac{1}{2} \left[ (p_{x,j} - k_0 \sigma_{z,j})^2 + p_{\perp,j}^2 \right] + \frac{\Omega}{2} \sigma_{x,j} + \frac{\delta}{2} \sigma_{z,j} + V_{\text{ext}}(\mathbf{r}_j), \quad (45)$$

and  $E_0, E_n$  are the corresponding energies. The quantity  $|\langle 0|F|n\rangle|^2$  is called the strength of the operator  $F$  relative to the state  $|n\rangle$ .

Some moments can be easily calculated by employing the closure relation and the commutation rules involving the Hamiltonian of the system. In the case of the dipole operator  $F = X$  one finds, for example, that the energy-weighted moment takes the well-known model-independent value (also called  $f$ -sum rule)

$$m_1(X) = \frac{1}{2} \langle 0|[X, [H, X]]|0\rangle = \frac{N}{2} \quad (46)$$

with  $N$  the total number of atoms. Notice that this sum rule is not affected by the spin terms in the Hamiltonian, despite the fact that the commutator of  $H$  with  $X$  explicitly depends on the spin-orbit coupling:

$$[H, X] = -i(P_x - k_0 \Sigma_z), \quad (47)$$

where  $P_x = \sum_j p_{x,j}$  is the total momentum of the gas along the  $x$  direction, and  $\Sigma_z = \sum_j \sigma_{z,j}$  is the total spin operator along  $z$ . Equation (47) actually reflects the fact that the equation of continuity (and hence in our case the dynamic behavior of the center-of-mass coordinate) is deeply influenced by the coupling with the spin variable.

Another important sum rule is the inverse energy-weighted sum rule (also called dipole polarizability). In the presence of harmonic trapping, this sum rule can be calculated in a straightforward way using the commutation relation

$$[H, P_x] = i\omega_x^2 X \quad (48)$$

<sup>d</sup>At finite temperature, the moments  $m_k$  should include the proper Boltzmann factors.<sup>42</sup>



and the closure relation. One finds

$$m_{-1}(X) = \frac{m_1(P_x)}{\omega_x^4} = \frac{N}{2\omega_x^2}. \quad (49)$$

Both sum rules (46) and (49) are insensitive to the presence of the spin terms in the single-particle Hamiltonian (45), as well as to the two-body interaction. This does not mean, however, that the dipole dynamics is not affected by the spin-orbit coupling. This effect is accounted for by another sum rule, particularly sensitive to the low-energy region of the excitation spectrum: the inverse cubic energy-weighted sum rule, for which we find the exact result

$$m_{-3}(X) = \frac{m_{-1}(P_x)}{\omega_x^4} = \frac{N}{2\omega_x^2} (1 + k_0^2 \chi_M), \quad (50)$$

where  $\chi_M$  corresponds to the magnetic polarizability already defined in Sec. 2.3, and given in terms of sum rules by  $\chi_M = 2m_{-1}(\Sigma_z)/N$ . It is worth mentioning that the above results for the sum rules  $m_1(X)$ ,  $m_{-1}(X)$  and  $m_{-3}(X)$  hold exactly for the Hamiltonian (6), including the interaction terms. Their validity is not restricted to the mean-field approximation and is ensured for both Bose and Fermi statistics, at zero as well as at finite temperature. In particular the sum rule  $m_{-3}(X)$ , being sensitive to the magnetic polarizability, is expected to exhibit a nontrivial temperature dependence across the BEC transition.

Equation (50) exploits the crucial role played by the spin-orbit coupling proportional to  $k_0$ . The effect is particularly important when the magnetic polarizability takes a large value. A large increase of  $\chi_M$  is associated with the occurrence of a dipole soft mode as can be inferred by taking the ratio between the inverse and cubic inverse energy-weighted sum rules  $m_{-1}(X)$  and  $m_{-3}(X)$ , yielding the rigorous upper bound

$$\omega_D^2 = \frac{m_{-1}(X)}{m_{-3}(X)} = \frac{\omega_x^2}{1 + k_0^2 \chi_M} \quad (51)$$

to the lowest dipole excitation energy. The value of  $\chi_M$  for a trapped BEC can be calculated in the same way as in uniform matter (see Sec. 2.3), with the difference that the condensate wave function is now provided by the solution of Eq. (43) rather than by the ansatz (8). Figure 10(a) shows the behavior of the magnetic polarizability in the plane-wave and the single-minimum phases as a function of the Raman coupling  $\Omega$ , calculated by numerically solving Eq. (43) in the presence of harmonic trapping along the  $x$  direction (red dashed lines), and by the relations (24) and (25) in

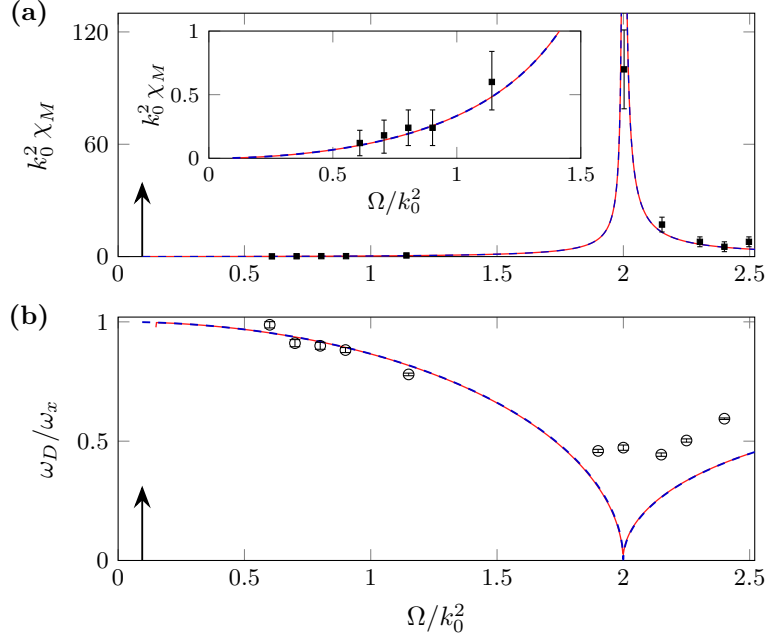


Fig. 10. **(a)** Magnetic polarizability  $\chi_M$  as a function of  $\Omega$  calculated in a trap (red solid lines) and in uniform matter using the density in the center of the trap (blue dashed lines). **(b)** Dipole frequency predicted by (51), using the values of  $\chi_M$  shown above, represented by the red solid lines and the blue dashed lines respectively. The parameters are  $k_0^2 = 2\pi \times 4.42$  kHz,  $\omega_x = 2\pi \times 45$  Hz, the scattering lengths  $a_{\uparrow\uparrow} = a_{\downarrow\downarrow} = 101.20 a_B$ ,  $a_{\uparrow\downarrow} = 100.94 a_B$ , where  $a_B$  is the Bohr radius, and the atomic mass of  $^{87}\text{Rb}$ . The density in the center of the trap is  $n \simeq 1.37 \times 10^{14} \text{ cm}^{-3}$ . The black squares and circles in the figures are the experimental data of Ref. 32. The black arrows indicate the transition between phases I and II.

uniform matter using the density in the center of the trap (blue solid lines). The choice of the parameters corresponds to the experimental conditions of Ref. 32. The black squares represent the magnetic polarizability extracted from the measurement of the oscillation amplitudes of some relevant quantities<sup>32</sup> (see the discussion in Sec. 4.2). Figure 10(b) shows the frequency of the dipole oscillation predicted from Eq. (51) using the same values of  $\chi_M$  presented in (a). It reveals important deviations from the trap frequency  $\omega_x$  caused by the spin-orbit coupling. The circles are the experimental results of Ref. 32. Far from the transition point at  $\Omega \simeq 2k_0^2$  the theoretical curves agree very well with the experimental data, while near the transition nonlinear effects play a major role, as discussed in Ref. 32. The lack of

data points in the region below the transition is due to the occurrence of a dynamic instability, which makes the observation of the dipole oscillation very difficult.<sup>48</sup>

#### 4.2. Dipole mode and oscillation amplitudes

The combined spin-orbit nature of the lowest dipole mode is also nicely revealed by the relative amplitudes of the oscillating values of the center-of-mass position ( $A_X$ ), the momentum ( $A_{P_x}$ ) and the spin polarization ( $A_{\Sigma_z}$ ). These amplitudes can be calculated in the present approach by writing the many-body oscillating wave function as

$$|\Psi(t)\rangle = e^{i\alpha(t)\delta P_x} e^{\beta(t)G} |0\rangle, \quad (52)$$

where  $\delta P_x = P_x - \langle P_x \rangle_0$  plays the role of the excitation operator,  $\langle \rangle_0$  denoting the expectation value on the ground state  $|0\rangle$ , while  $G$  represents the restoring force defined by the commutation relation  $[H, G] = \delta P_x$ , and  $\alpha, \beta$  are time-dependent parameters. The equations governing the time evolution of these parameters can be obtained through a variational Lagrange procedure; at the lowest order in  $\alpha$  and  $\beta$  they read

$$\dot{\alpha}(t) = -\beta(t), \quad (53)$$

$$\dot{\beta}(t) = \frac{\omega_x^2}{1 + k_0^2 \chi_M} \alpha(t). \quad (54)$$

The time dependence of the relevant quantities  $\langle X \rangle$ ,  $\langle P_x \rangle$  and  $\langle \Sigma_z \rangle$  can be obtained by solving Eqs. (53) and (54). The relations between the spin, the center-of-mass and the momentum oscillation amplitudes eventually take the useful form

$$A_{\Sigma_z} = A_X \frac{\omega_x k_0 \chi_M}{\sqrt{1 + k_0^2 \chi_M}}, \quad (55)$$

$$\frac{A_{P_x}}{k_0} = A_{\Sigma_z} \frac{1 + k_0^2 \chi_M}{k_0^2 \chi_M}. \quad (56)$$

The connection between the momentum and spin amplitudes has been already pointed out in Ref. 32 (see Fig. 4 therein). It provides a practical way to determine experimentally the magnetic polarizability  $\chi_M$ . Near the transition point between the plane-wave and the single-minimum phase the ratio  $A_{\Sigma_z}/A_X$  between the spin and the center-of-mass amplitudes diverges like  $\sqrt{\chi_M}$ , in analogy with the behavior exhibited by the ratio between the spin and the density amplitudes in the propagation of sound (see Eq. (42)).

It is worth pointing out that the results (55)–(56), as well as the upper bound of the excitation frequency (51), are expected to be accurate when the Raman coupling  $\Omega$  is larger than the trapping frequency  $\omega_x$ . Instead, in the opposite limit  $\Omega \ll \omega_x$ , the lowest mode is mainly a spin oscillation, which does not exhibit any significant coupling to the center-of-mass motion. The corresponding frequency can be estimated with a sum-rule approach by considering the ratio  $m_1(\Sigma_z)/m_{-1}(\Sigma_z)$  of the moments of the spin operator  $\Sigma_z$ . The excitation frequency calculated in this way is found to vanish linearly with  $\Omega$ . Finally, in the intermediate regime between the two limits discussed above, one can define  $F = P_x + \eta k_0 \Sigma_z$  and use the ansatz  $\delta F = F - \langle F \rangle_0$  for the operator exciting the dipole oscillation, where the value of the variational parameter  $\eta$  is found by minimizing the estimate  $m_1(F)/m_{-1}(F)$  for the excitation frequency. The corresponding oscillation amplitudes of the relevant physical quantities can be calculated by a procedure analogous to the one discussed above.<sup>30</sup>

#### 4.3. Hydrodynamic formalism

A useful approach to describe the phonon regime in the excitation spectrum of a superfluid is provided by hydrodynamic theory. For a spinor BEC this theory can be derived by writing the spin-up and spin-down components of the order parameter in terms of their modulus and phase.<sup>33,34</sup> In the resulting equations the quantum pressure terms can be safely neglected in the phonon regime, characterized by long wavelengths and low frequencies. Furthermore, since the phonon frequencies are much smaller than the gap between the two branches of the excitation spectrum, which is of the order of  $\Omega$ , the relative phase of the two spin components is locked ( $\phi_\uparrow = \phi_\downarrow$ ). As a consequence, the relevant hydrodynamic equations reduce to the equations for the change in the total density  $\delta n$  and in the phase  $\delta\phi = \delta\phi_\uparrow = \delta\phi_\downarrow$ . Assuming for simplicity  $g_{\uparrow\downarrow} = g$ , these two equations assume the simple form

$$\frac{\partial}{\partial t} \delta n + \nabla_\perp \cdot (n \nabla_\perp \delta\phi) + \frac{m}{m^*} \partial_x (n \partial_x \delta\phi) = 0 \quad (57)$$

and

$$\frac{\partial}{\partial t} \delta\phi + \delta\mu = 0, \quad (58)$$

with  $m/m^*$  given by Eqs. (4) and (5) and  $\delta\mu = g\delta n$ . Notice that, due to the assumption  $g_{\uparrow\downarrow} = g$ , the above hydrodynamic picture can describe the dynamics only in the plane-wave and the single-minimum phases (the

investigation of the phonon modes in the stripe phase requires a more sophisticated calculation, see Sec. 5). Remarkably, the equation of continuity (57) is crucially affected by the spin-orbit coupling. This follows from the fact that the current is not simply given by the canonical momentum operator, as happens in usual superfluids, but contains an additional spin contribution, accounted for, in Eq. (57), through the effective mass term. The current density operator should actually satisfy the continuity equation  $[H, \rho(\mathbf{r})] = i\nabla \cdot \mathbf{j}$ , where  $\rho(\mathbf{r}) = \sum_j \delta(\mathbf{r} - \mathbf{r}_j)$  is the total density operator. By explicitly carrying out the commutator one identifies the current as  $\mathbf{j}(\mathbf{r}) = \mathbf{p}(\mathbf{r}) - k_0 \sigma_z(\mathbf{r}) \hat{\mathbf{e}}_x$ , where  $\mathbf{p}(\mathbf{r}) = \sum_j [\mathbf{p}_j \delta(\mathbf{r} - \mathbf{r}_j) + \text{H.c.}]/2$  and  $\sigma_z(\mathbf{r}) = \sum_j \sigma_{z,j} \delta(\mathbf{r} - \mathbf{r}_j)$  are the momentum and spin-density operators, respectively. This expression for the current explicitly reveals the presence of a gauge field associated to the vector potential  $\mathbf{A} = k_0 \sigma_z \hat{\mathbf{e}}_x$ . It is worth noticing that at equilibrium the momentum and spin-dependent terms exactly compensate each other, yielding  $\langle \mathbf{j}(\mathbf{r}) \rangle = 0$ . The presence of the spin term in the current also reflects the violation of Galilean invariance in the spin-orbit Hamiltonian.<sup>48</sup>

Combining (57) and (58) one finds the following equation for the density:

$$\frac{\partial^2}{\partial t^2} \delta n = g \left[ \nabla_\perp \cdot (n \nabla_\perp \delta n) + \frac{m}{m^*} \partial_x (n \partial_x \delta n) \right]. \quad (59)$$

In uniform matter, characterized by a constant density  $n = \bar{n}$ , Eq. (59) yields the relation  $c^2 = g\bar{n}/m^*$  for the sound velocity along the  $x$  direction, consistent with the results (37) and (38) for  $g_{\uparrow\downarrow} = g$ . In the presence of harmonic trapping, where the equilibrium density profile is given by an inverted parabola, the solutions of the hydrodynamic equation (59) coincide with those one finds for usual BECs, with the simple replacement of the trap frequency  $\omega_x$  with  $\omega_x \sqrt{m/m^*}$ . This gives the result  $\omega_D = \omega_x \sqrt{m/m^*}$  for the dipole frequency, which is consistent with the estimate (51) based on a sum-rule approach, once the relation (26) between the effective mass and the magnetic polarizability (holding for  $G_2 = 0$ ) is taken into account. Equation (59) also shows that, for any other hydrodynamic mode involving a motion of the gas along the  $x$  axis, a similar effect of strong reduction of the frequency close to the second-order transition should be expected. This is the case, for example, of the scissors mode for deformed traps in the  $x$ - $y$  or  $x$ - $z$  plane, where the collective frequency takes the form  $\sqrt{(m/m^*)\omega_x^2 + \omega_y^2}$  and  $\sqrt{(m/m^*)\omega_x^2 + \omega_z^2}$  respectively.

## 5. Static and Dynamic Properties of the Stripe Phase

The stripe phase is doubtlessly the most intriguing phase appearing in the phase diagram of Sec. 2. It has been the object of several recent theoretical investigations.<sup>29,35,49–57</sup> As we already pointed out, the stripe phase is characterized by the spontaneous breaking of two continuous symmetries. The breaking of gauge symmetry yields superfluidity, while the breaking of translational invariance is responsible for the occurrence of a crystalline structure. The simultaneous presence of these two broken symmetries is typical of supersolids.<sup>28,58–60</sup> As we shall see, it is at the origin of the appearance of two gapless excitations as well as of a band structure in the excitation spectrum.<sup>35</sup>

Some important properties of the ground state and the dynamics of the stripe phase in uniform matter will be discussed in Secs. 5.1 and 5.2. Many relevant quantities that we will consider, such as the contrast of the density modulations (15), will turn out to depend crucially on the value of the Raman coupling  $\Omega$ . Therefore, in order to enhance the effects of the presence of the stripes one needs to use relatively large values of  $\Omega$ . On the other hand, the stripe phase is favored only in a range of low values of the Raman coupling lying below the transition frequency  $\Omega^{(I-II)}$ . In the following we will consider configurations with relatively large values of the parameter  $G_2$  which, as can be seen from Eq. (21), allow to obtain a significant increase of the critical value of  $\Omega$ . This is not, however, the situation in current experiments with  $^{87}\text{Rb}$  atoms,<sup>18,32</sup> where  $G_2$  is instead extremely small. In Sec. 5.3 we will illustrate a procedure to increase the value of  $G_2$  with available experimental techniques.

### 5.1. Ground state and excitation spectrum

In Sec. 2.2 the ground state in the stripe phase has been described by means of an approximated wave function, based on the ansatz (8), which takes into account only first-order harmonic terms. The exact wave function includes also higher-order harmonics, whose appearance is a consequence of the nonlinearity of the Gross-Pitaevskii theory. It can be written in the form

$$\begin{pmatrix} \psi_{0\uparrow} \\ \psi_{0\downarrow} \end{pmatrix} = \sqrt{\bar{n}} \sum_{\bar{K}} \begin{pmatrix} a_{-k_1+\bar{K}} \\ -b_{-k_1+\bar{K}} \end{pmatrix} e^{i(\bar{K}-k_1)x}, \quad (60)$$

where  $k_1 = \pi/d$  is related to the period  $d$  of the stripes,  $\bar{K} = 2nk_1$ , with  $n = 0, \pm 1, \dots$ , are the reciprocal lattice vectors, while  $a_{-k_1+\bar{K}}$  and  $b_{-k_1+\bar{K}}$

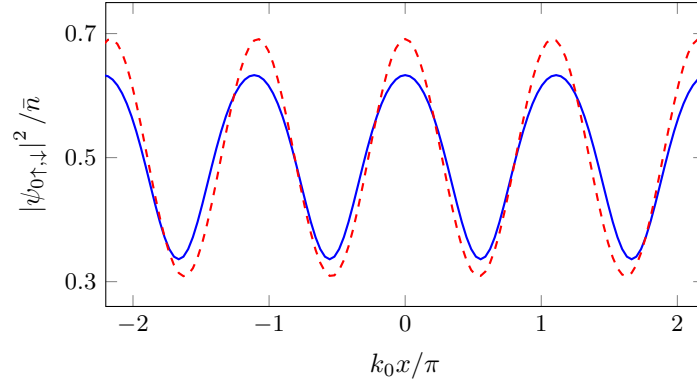


Fig. 11. Density profile in the stripe phase along the  $x$  direction, calculated within the first-order harmonic approximation (8) (red dashed line) and from Eq. (60) including the higher-order harmonics (blue solid line). The parameters are  $\Omega/k_0^2 = 1.0$ ,  $G_1/k_0^2 = 0.3$ , and  $G_2/k_0^2 = 0.08$ , yielding the transition frequency  $\Omega^{(1-\Pi)}/k_0^2 \simeq 1.3$ .

are expansion coefficients to be determined, together with the value of  $k_1$ , by a procedure of minimization of the mean-field energy functional (7). The energy minimization gives rise to the presence of terms with opposite phase ( $e^{\pm i k_1 x}$ ,  $e^{\pm 3 i k_1 x}$ , ...), responsible for the density modulations and characterized by the symmetry condition  $a_{-k_1 + \bar{K}} = b_{k_1 - \bar{K}}^*$ , causing the vanishing of the spin polarization  $\langle \sigma_z \rangle$ . Figure 11 shows an example of density profile in the stripe phase, calculated for a configuration with relatively large values of  $G_2$  and  $\Omega/k_0^2$  in order to emphasize the contrast in the density modulations.

As in the case of the uniform phases, also in the stripe phase we can evaluate the elementary excitations by the standard Bogoliubov approach, writing the deviations of the order parameter with respect to equilibrium as

$$\Psi = e^{-i\mu t} \left[ \begin{pmatrix} \psi_{0\uparrow} \\ \psi_{0\downarrow} \end{pmatrix} + \begin{pmatrix} u_{\uparrow}(\mathbf{r}) \\ u_{\downarrow}(\mathbf{r}) \end{pmatrix} e^{-i\omega t} + \begin{pmatrix} v_{\uparrow}^*(\mathbf{r}) \\ v_{\downarrow}^*(\mathbf{r}) \end{pmatrix} e^{i\omega t} \right] \quad (61)$$

and solving the corresponding linearized time-dependent Gross-Pitaevskii equations. The equations are conveniently solved by expanding  $u_{\uparrow,\downarrow}(\mathbf{r})$  and  $v_{\uparrow,\downarrow}(\mathbf{r})$  in the Bloch form in terms of the reciprocal lattice vectors:

$$u_{\mathbf{q}\uparrow,\downarrow}(\mathbf{r}) = e^{-i k_1 x} \sum_{\bar{K}} U_{\mathbf{q}\uparrow,\downarrow \bar{K}} e^{i \mathbf{q} \cdot \mathbf{r} + i \bar{K} x}, \quad (62)$$

$$v_{\mathbf{q}\uparrow,\downarrow}(\mathbf{r}) = e^{i k_1 x} \sum_{\bar{K}} V_{\mathbf{q}\uparrow,\downarrow \bar{K}} e^{i \mathbf{q} \cdot \mathbf{r} - i \bar{K} x}, \quad (63)$$

where  $\mathbf{q}$  is the wave vector of the excitation. This ansatz can also be used to calculate the density and spin-density dynamic response function, similarly to what we did in Sec. 3.1, by adding to the Hamiltonian a perturbation proportional to  $e^{i(\mathbf{q}\cdot\mathbf{r}-\omega t)+\eta t}$  and  $\sigma_z e^{i(\mathbf{q}\cdot\mathbf{r}-\omega t)+\eta t}$  with  $\eta \rightarrow 0^+$ , respectively.

The spectrum of the elementary excitations in the stripe phase is reported in Fig. 12 for the same parameters used in Fig. 11. We have considered both excitations propagating in the  $x$  direction orthogonal to the stripes (labelled with the wave vector  $q_x$ ) and in the transverse directions parallel to the stripes (identified by the wave vector  $q_\perp$ ). A peculiar feature, distinguishing the stripe phase from the other uniform phases, is the occurrence of two gapless bands. The excitation energies along the  $x$  direction vanish at the Brillouin wave vector  $q_B = 2k_1$ , which is a usual situation in crystals. A similar double gapless band structure has been predicted recently in condensates with soft-core, finite-range interactions.<sup>37,38,61</sup>

In Fig. 13 we compare the sound velocities of the two gapless branches in the longitudinal ( $c_x$ ) and transverse ( $c_\perp$ ) directions. We find that  $c_x$  is always smaller than  $c_\perp$ , reflecting the inertia of the flow caused by the presence of the stripes. The value of  $c_\perp$  in the second band (second sound) is well reproduced by the Bogoliubov expression  $\sqrt{2G_1}$  (equal to  $0.78 k_0$  in our case) for the sound velocity. Notice that the sound velocity in the first band (first sound) becomes lower and lower as the Rabi frequency increases, approaching the transition to the plane-wave phase. The Bogoliubov solutions in the stripe phase exist also for values of  $\Omega$  larger than the critical value  $\Omega^{(I-II)} = 1.3 k_0^2$ , due to the first-order nature of the transition (effect of metastability).

## 5.2. Static structure factor and static response function

The nature of the excitation bands can be understood by calculating the static structure factors for the density and the spin-density operators, which can be written as

$$S(\mathbf{q}) = N^{-1} \sum_{\ell} |\langle 0 | \rho_{\mathbf{q}} | \ell \rangle|^2 \quad (64)$$

and

$$S_{\sigma}(\mathbf{q}) = N^{-1} \sum_{\ell} |\langle 0 | \sigma_{z,\mathbf{q}} | \ell \rangle|^2 \quad (65)$$

respectively. In these equations  $\rho_{\mathbf{q}} = \sum_j e^{i\mathbf{q}\cdot\mathbf{r}_j}$  and  $\sigma_{z,\mathbf{q}} = \sum_j \sigma_{z,j} e^{i\mathbf{q}\cdot\mathbf{r}_j}$  are the  $\mathbf{q}$  components of the above-mentioned operators, while  $\ell$  is the band



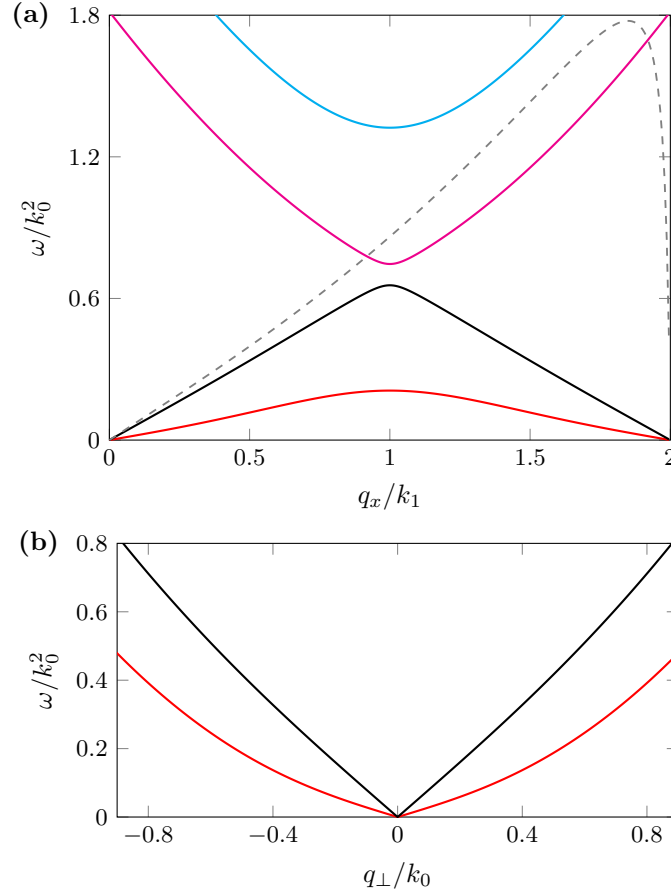


Fig. 12. **(a)**. Lowest four excitation bands (solid lines) along the  $x$  direction ( $q_{\perp} = 0$ ). The dashed line corresponds to the Feynman relation  $\omega = q_x^2/2S(q_x)$ . **(b)**. Lowest two excitation bands in the transverse direction ( $q_x = 0$ ). The parameters are the same as in Fig. 11.

index. In Fig. 14 we show the static structure factors for wave vectors along the  $x$  axis, as well as the contributions to the total sum coming from the two gapless branches ( $\ell = 1, 2$ ). The figure clearly shows that, at small  $q_x$ , the lower branch is basically a spin excitation, while the upper branch is a density mode. The density nature of the upper branch, at small  $q_x$ , is further confirmed by the comparison with the Feynman relation  $\omega = q_x^2/2S(q_x)$  (see Fig. 12(a)). A two-photon Bragg scattering experiment with laser frequencies far from resonance, being sensitive to the density response,

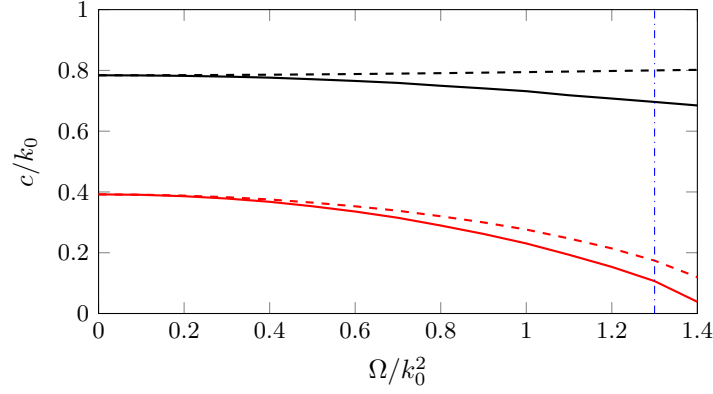


Fig. 13. Sound velocities in the first (red) and second (black) bands along the  $x$  ( $c_x$ , solid lines) and transverse ( $c_\perp$ , dashed lines) directions as a function of  $\Omega$ . The blue dash-dotted line represents the transition from the stripe phase to the plane-wave phase. The values of the parameters  $G_1/k_0^2$  and  $G_2/k_0^2$  are the same as in Fig. 11.

will consequently excite only the upper branch at small  $q_x$ . Bragg scattering experiments actually measure the imaginary part of the response function, a quantity which, at enough low temperature, can be identified with the  $T = 0$  value of the dynamic structure factor  $S(q_x, \omega) = \sum_\ell |\langle 0 | \rho_{q_x} | \ell \rangle|^2 \delta(\omega - \omega_{\ell 0})$ , where  $\omega_{\ell 0}$  is the excitation frequency of the  $\ell$ -th state.<sup>42</sup> Notice that, differently from  $S(q_x)$ , the spin structure factor  $S_\sigma(q_x)$  does not vanish as  $q_x \rightarrow 0$ , being affected by the higher energy bands as a consequence of the Raman term in Hamiltonian (2). As  $q_x$  increases, the lower branch actually reveals a hybrid character and, when approaching the Brillouin wave vector  $q_B = 2k_1$ , it is responsible for the divergent behavior of the density static structure factor (see Fig. 14(a)), which is again a typical feature exhibited by crystals.

It is worth pointing out that the occurrence of two gapless excitations is not by itself a signature of supersolidity and is exhibited also by uniform mixtures of BECs without spin-orbit and Raman couplings<sup>62</sup> as well as by the plane-wave phase of the Rashba Hamiltonian with  $SU(2)$ -invariant interactions ( $G_2 = 0$ ).<sup>63–65</sup> Only the occurrence of a band structure, characterized by the vanishing of the excitation energy and by the divergent behavior of the structure factor at the Brillouin wave vector, can be considered an unambiguous evidence of the density modulations characterizing the stripe phase. The divergent behavior near the Brillouin zone is even more pronounced (see Fig. 15) if one investigates the static response func-

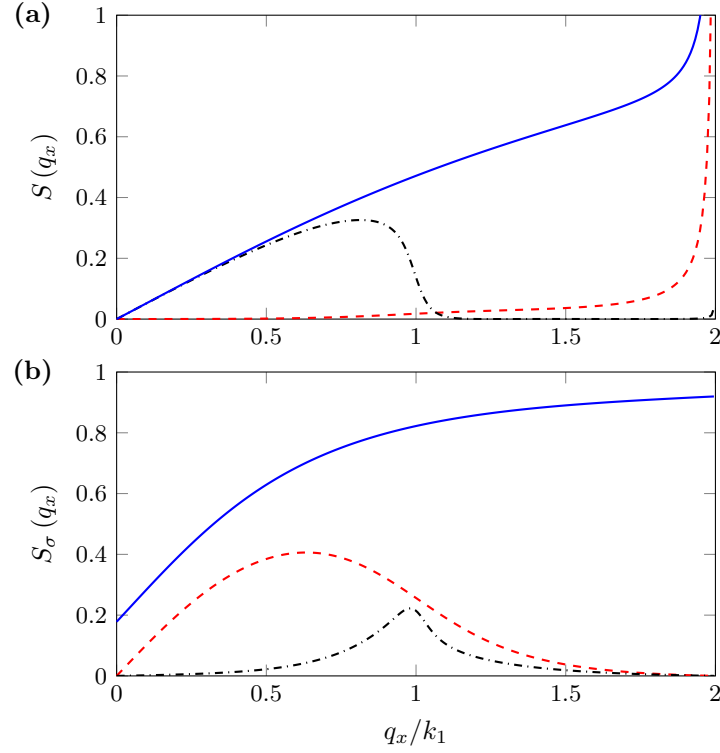


Fig. 14. Density **(a)** and spin-density **(b)** static structure factor as a function of  $q_x$  (blue solid line). The contributions of the first (red dashed line) and second (black dash-dotted line) bands are also shown. The parameters are the same as in Fig. 11.

tion

$$\chi(q_x) = 2N^{-1} \sum_{\ell} \frac{|\langle 0 | \rho_{q_x} | \ell \rangle|^2}{\omega_{\ell 0}}, \quad (66)$$

proportional to the inverse energy-weighted moment of the dynamic structure factor.

The divergent behaviors of  $S(q_x)$  and  $\chi(q_x)$  can be rigorously proven using the Bogoliubov<sup>66</sup> and the uncertainty principle<sup>45,46</sup> inequalities applied to systems with spontaneously broken continuous symmetries. These inequalities are based, respectively, on the relations

$$m_{-1}(F)m_1(G) \geq |\langle [F, G] \rangle|^2 \quad (67)$$

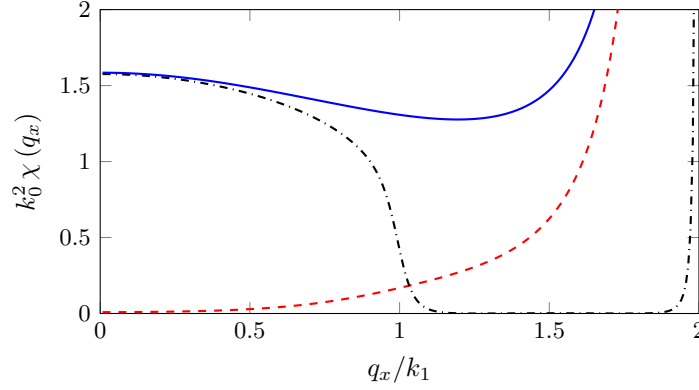


Fig. 15. Static response as a function of  $q_x$  (blue solid line). The contributions of the first (red dashed line) and second (black dash-dotted line) bands are also shown. The parameters are the same as in Fig. 11.

and

$$m_0(F)m_0(G) \geq |\langle [F, G] \rangle|^2 \quad (68)$$

involving the  $k$ -th moments  $m_k(\mathcal{O}) = \sum_{\ell} (|\langle 0|\mathcal{O}|\ell\rangle|^2 + |\langle 0|\mathcal{O}^\dagger|\ell\rangle|^2) \omega_{\ell 0}^k$  of the  $\ell$ -th strengths of the operators  $F = \sum_j e^{iq_x x_j}$  and  $G = \sum_j (p_{x,j} e^{-i(q_x - q_B)x_j} + \text{H.c.})/2$ , with  $q_B = 2k_1$  the Brillouin wave vector defined above. The commutator  $\langle [F, G] \rangle = q_x N \langle e^{iq_B x} \rangle$ , entering the right-hand side of the inequalities, coincides with the relevant crystalline order parameter and is proportional to the density modulations of the stripes. The moments  $m_{-1}(F)$  and  $m_0(F)$  are instead proportional to the static response  $\chi(q_x)$  and to the static structure factor  $S(q_x)$ , respectively. It is not difficult to show that the moments  $m_1(G)$  and  $m_0(G)$  are proportional, respectively, to  $(q_x - q_B)^2$  and to  $|q_x - q_B|$  as  $q_x \rightarrow q_B$  due to the translational invariance of the Hamiltonian. This causes the divergent behaviors  $S(q_x) \propto 1/|q_x - q_B|$  and  $\chi(q_x) \propto 1/(q_x - q_B)^2$  with a weight factor proportional to the square of the order parameter. The value of the crystalline order parameter  $\langle e^{iq_B x} \rangle$  is larger for larger values of  $\Omega$ . For this reason it is useful to work with large values of the spin interaction parameter  $G_2$ , allowing for large values of the Raman coupling.<sup>e</sup> The experimental achievement of configurations with relatively large  $G_2$  will be the subject of the next subsection.

<sup>e</sup>For <sup>87</sup>Rb the value of  $G_2$  is small and the divergency effect in  $S(q_x)$  is weak. In this case, the sound velocity of the lowest band is small and the dispersion practically exhibits a  $q^2$ -like behavior at small  $q$ .

### 5.3. Experimental perspectives for the stripe phase

As we have already anticipated, there is still no experimental evidence for the periodic modulations of the density profile in the stripe phase. The main reason is that, in the conditions of current experiments with spin-orbit-coupled  $^{87}\text{Rb}$  BECs,<sup>18,32</sup> the contrast and the wavelength of the fringes are too small to be revealed. Another problem originates from the smallness of the difference  $\Delta\mu$  between the chemical potentials in the plane-wave and the stripe phases, which, assuming  $g_{\uparrow\uparrow} = g_{\downarrow\downarrow}$ , is given by  $\Delta\mu = 2G_2$  in the  $\Omega = 0$  limit, and becomes even smaller at finite  $\Omega$ . As a consequence, a tiny magnetic field (arising, for example, from external fluctuations) can easily bring the system into the spin-polarized plane-wave phase.

In Ref. 67 we have proposed a procedure to make the experimental detection of the fringes a realistic perspective, improving their contrast and their wavelength, and increasing the stability of the stripe phase against magnetic fluctuations. The idea is to trap the atomic gas in a 2D configuration, with tight confinement of the spin-up and spin-down components around two different positions, displaced by a distance  $d$  along the  $z$  direction. This configuration can be realized with a trapping potential of the form

$$V_{\text{ext}}(z) = \frac{\omega_z^2}{2} \left( z - \frac{d}{2} \sigma_z \right)^2 \quad (69)$$

with a sufficiently large value of  $\omega_z$ . As a consequence of these trapping conditions, the overlap of the densities of the two spin components can be significantly quenched, and thus the effective interspecies coupling is reduced with respect to the intraspecies couplings. This yields a value of the parameter  $\gamma$  larger than in the  $d = 0$  case, and consequently the critical Raman coupling  $\Omega^{(\text{I-II})}$  can significantly increase (see Eq. (21)), allowing for the realization of the striped configuration with a high fringe contrast (15).<sup>f</sup>

Quantitative predictions for the novel configuration discussed above can be obtained by solving numerically the 3D Gross-Pitaevskii equation. In Figs. 16 and 17 we show the results for a gas of  $N = 4 \times 10^4$   $^{87}\text{Rb}$  atoms confined by an harmonic potential with frequencies  $(\omega_x, \omega_y, \omega_z) = 2\pi \times (25, 100, 2500)$  Hz, the scattering lengths equal to those reported in Sec. 2,  $k_0 = 5.54 \mu\text{m}^{-1}$  and  $E_r = h \times 1.77$  kHz consistent with Ref. 18. Figure 16

<sup>f</sup>Another important consequence is that, due to the increase of the value of  $\gamma$ , the critical density  $n^{(c)}$  can be significantly lowered with respect to the value in the  $d = 0$  case, becoming of more realistic achievement in future experiments.

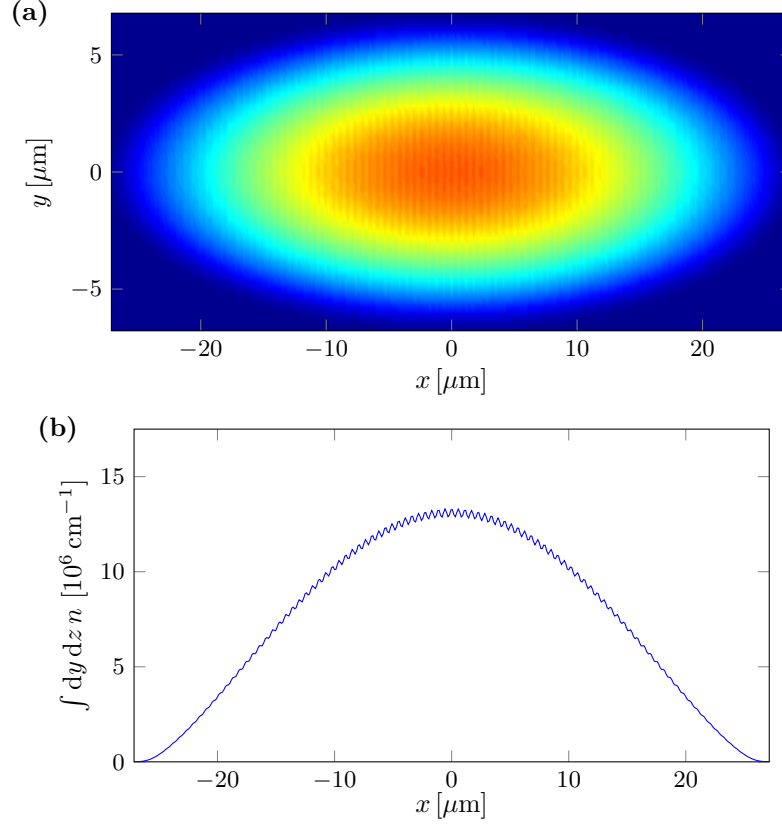


Fig. 16. Integrated density profiles  $\int dz n$  (a) and  $\int dy dz n$  (b) in the stripe phase, evaluated in the conditions described in the text, and without separation of the traps for the two spin components ( $d = 0$ ).

corresponds to  $d = 0$ , while Fig. 17 corresponds to  $d = a_z = 0.22 \mu\text{m}$ ,  $a_z$  being the harmonic oscillator length along  $z$ . In both Figs. 16 and 17 we have chosen values of the Raman coupling equal to one half the critical value needed to enter the plane-wave phase, in order to ensure more stable conditions for the stripe phase. This corresponds to  $\Omega = 0.095 E_r$  in Fig. 16 and to  $\Omega = 1.47 E_r$  in Fig. 17. The density plotted in the top panels corresponds to the 2D density, obtained by integrating the full 3D density along the  $z$  direction; in the bottom panels we show the double integrated density  $\int dy dz n$  as a function of the most relevant  $x$  variable. The figures clearly show that in the conditions of almost equal coupling

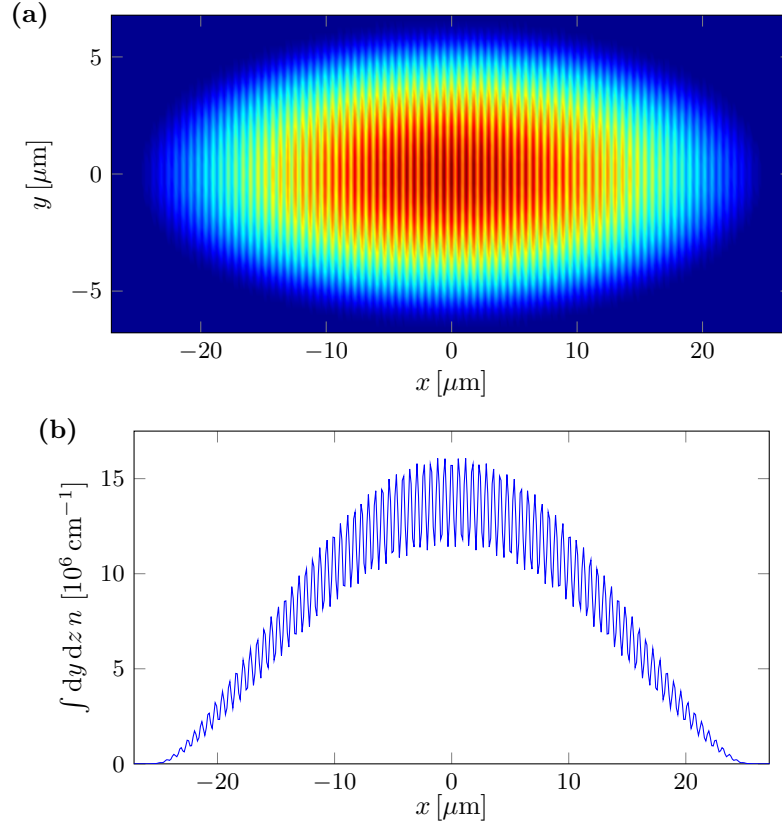


Fig. 17. Integrated density profiles  $\int dz n$  (a) and  $\int dy dz n$  (b) in the stripe phase, evaluated in the conditions described in the text, and with traps separated along  $z$  by a distance  $d = a_z$ , which helps increasing the visibility of the fringes with respect to Fig. 16.

constants (Fig. 16) the density modulations are very small, while their effect is strongly amplified in Fig. 17, where the interspecies coupling is reduced with respect to the intraspecies values.

The suggested procedure has also the positive effect of making the stripe phase more robust against fluctuations of external magnetic fields. Indeed, the reduction of the interspecies coupling and the increase of the local density, due to the tight axial confinement, yield a significant increase of the energy difference between the stripe and the plane-wave phases. For example, in the case considered above, for the configuration with a  $d = a_z$  displacement of the two spin layers (Fig. 17) a magnetic detuning of about

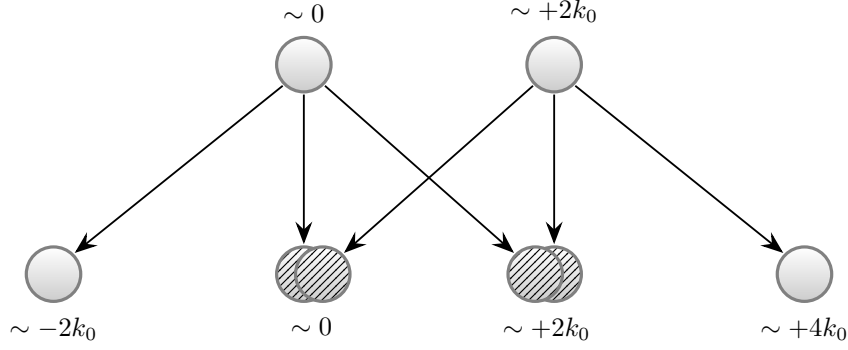


Fig. 18. Schematic description of the splitting of the spin-down component of the stripe wave function into different momentum components caused by a  $\pi/2$  Bragg pulse transferring momentum  $2k_1 - \epsilon$ .

$0.35 E_r$  is required to bring the system into the spin-polarized phase; in the absence of displacement (Fig. 16) the critical value for the magnetic detuning is instead much smaller ( $\sim 0.001 E_r$ ).<sup>68</sup>

Let us finally address the problem of the small spatial separation of the fringes, given by  $\pi/k_1$ , which turns out to be of the order of a fraction of a micron in standard conditions. One possibility to increase the wavelength of the stripes is to lower the value of  $k_0$  by using lasers with a smaller relative incident angle. In the following we discuss a more drastic procedure which consists of producing, after the realization of the stripe phase, a  $\pi/2$  Bragg pulse with a short time duration (smaller than the time  $1/E_r$  fixed by the recoil energy), followed by the sudden release of the trap. This pulse can transfer to the condensate a momentum  $k_B$  or  $-k_B$  along the  $x$  direction, where  $k_B$  is chosen equal to  $2k_1 - \epsilon$  with  $\epsilon$  small compared to  $k_1$ . The  $\pi/2$  pulse has the effect of splitting the condensate into various pieces, with different momenta. The situation is schematically shown in Fig. 18 for the spin-down component, where the initial condensate wave function, which in the stripe phase is a linear combination with canonical momenta  $\pm k_1$ , corresponding to momenta  $k_0 - k_1$  and  $k_0 + k_1$  in the laboratory frame, after the Bragg pulse will be decomposed into six pieces. Two of them, those labeled in the lower part of the figure with momentum  $\sim 0$ , will be practically at rest after the pulse and are able to interfere with fringes of wavelength  $2\pi/\epsilon$ , which can easily become large and visible *in situ*. It is worth noticing that these two latter pieces originate from the two different momentum components of the order parameter (8) in the stripe phase and



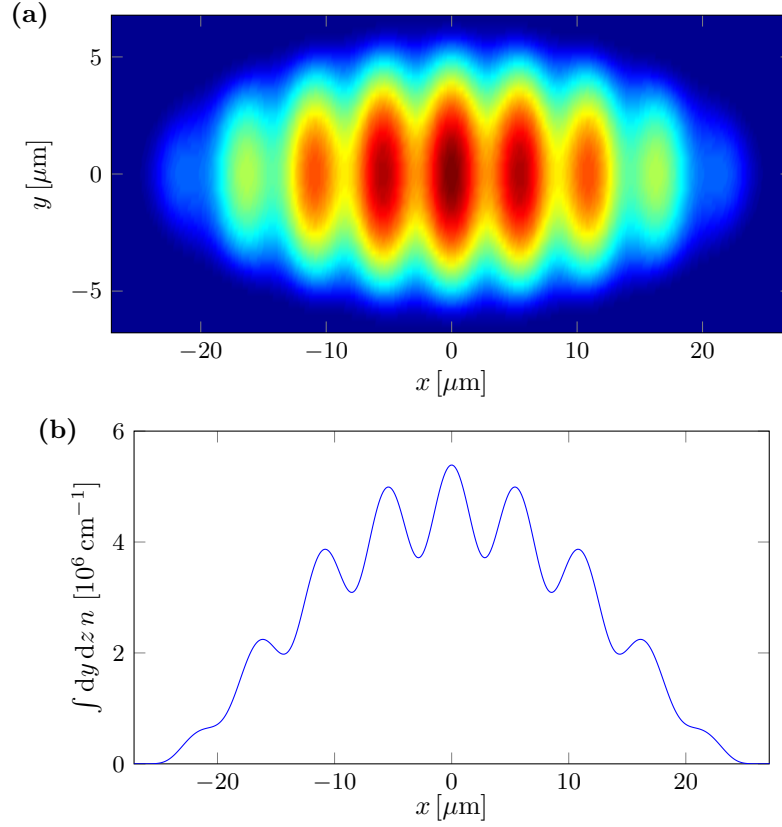


Fig. 19. Integrated density profiles  $\int dz n$  (a) and  $\int dy dz n$  (b) in the stripe phase, in the same conditions as Fig. 17, after the application of a  $\pi/2$  Bragg pulse with transferred momentum  $k_B = 1.8 k_1$ .

involve 1/3 of the total number of atoms. The corresponding interference effect would be consequently absent in the plane-wave phase, where only one momentum component characterizes the order parameter. The other pieces produced by the Bragg pulse carry much higher momenta and will fly away rapidly after the release of the trap and of the laser fields. In Fig. 19 we show a typical behavior of the density profile obtained by modifying the condensate wave function in momentum space according to the prescription discussed above.

## 6. Conclusion

In this review we have illustrated some relevant static and dynamic properties of spin-orbit-coupled Bose–Einstein condensates in the simplest realization of a spin-1/2 configuration, characterized by equal Rashba and Dresselhaus couplings and vanishing or small magnetic detuning. The phase diagram of these Bose–Einstein condensates is characterized by the existence of three phases: the stripe, the plane-wave and the single-minimum phase. These phases merge in a characteristic tricritical point. The phase transition between the stripe and the plane-wave phase has a first-order nature, while the transition between the plane-wave and the single-minimum phase is of second order and is characterized by a divergent behavior of the magnetic polarizability. The stripe phase exhibits typical density modulations, which are the consequence of a mechanism of spontaneous breaking of translational invariance. The three phases discussed in the present paper exhibit interesting dynamical features, like the suppression of the dipole oscillation frequency in the presence of harmonic trapping and of the sound velocity close to the second-order phase transition, the appearance of a roton minimum in the plane-wave phase and the occurrence of a double gapless band structure in the excitation spectrum of the stripe phase. Some of these features have already been confirmed in recent experiments. Finally, we have discussed a procedure for the experimental exploration of the intriguing physics of the stripe phase, opening new perspectives for the identification of supersolid phenomena in ultracold atomic gases.

## Acknowledgments

We wish to thank Lev P. Pitaevskii for many useful and stimulating discussions. This work has been supported by ERC through the QGBE grant and by Provincia Autonoma di Trento. The Centre for Quantum Technologies is a Research Centre of Excellence funded by the Ministry of Education and National Research Foundation of Singapore.

### A.1. Coefficients in the response function

The coefficients in the response function (33) can be expressed as follows. In phase II:

$$\begin{aligned}
a &= -\frac{q^4}{4} + \left[ (k_0^2 + 3k_1^2) \cos^2 \alpha - 2(k_0^2 - G_2) + \frac{2G_2 k_1^2}{k_0^2} \right] q^2 \\
&\quad + 4(k_0^2 - 2G_2) \left[ (k_0^2 - k_1^2) \cos^2 \alpha - k_0^2 + \frac{2G_2 k_1^2}{k_0^2} \right], \\
b_0 &= \frac{q^8}{16} - [(k_0^2 + k_1^2) \cos^2 \alpha - k_0^2 - G_1 + G_2] \frac{q^6}{2} \\
&\quad + \left\{ (k_0^2 - k_1^2)^2 \cos^4 \alpha \right. \\
&\quad \left. - 2[k_0^2(k_0^2 - k_1^2) + G_1(k_0^2 + 3k_1^2) - G_2(k_0^2 - 5k_1^2)] \cos^2 \alpha \right. \\
&\quad \left. + k_0^2(k_0^2 - 2G_2) + 4G_1(k_0^2 - G_2) + 2(k_0^2 - 2G_1 - 2G_2) \frac{G_2 k_1^2}{k_0^2} \right\} q^4 \\
&\quad - 8(k_0^2 - 2G_2) \left[ (k_0^2 - k_1^2) \left( G_1 + \frac{G_2 k_1^2}{k_0^2} \right) \cos^2 \alpha \right. \\
&\quad \left. - G_1 k_0^2 - (k_0^2 - 2G_1 - 2G_2) \frac{G_2 k_1^2}{k_0^2} \right] q^2, \\
b_1 &= q^4 + 4[(k_0^2 - k_1^2) \cos^2 \alpha + 2(G_1 + G_2)] q^2 + 16(k_0^2 - 2G_2)(k_0^2 - k_1^2) \frac{G_2}{k_0^2}, \\
b_2 &= -\frac{q^4}{2} - 2[(k_0^2 - 3k_1^2) \cos^2 \alpha + k_0^2 + G_1 - G_2] q^2 \\
&\quad - 4(k_0^2 - 2G_2) \left( k_0^2 - \frac{2G_2 k_1^2}{k_0^2} \right),
\end{aligned}$$

with  $k_1$  given by (17). In phase III:

$$\begin{aligned}
a &= -\frac{q^4}{4} - (\Omega - k_0^2 \cos^2 \alpha + 2G_2) q^2 - \Omega [\Omega - 2(k_0^2 \cos^2 \alpha - 2G_2)], \\
b_0 &= \frac{q^8}{16} + [\Omega - 2(k_0^2 \cos^2 \alpha - G_1 - G_2)] \frac{q^6}{4} \\
&\quad + [\Omega^2 - 4(k_0^2 \cos^2 \alpha - 2G_1 - G_2) \Omega \\
&\quad + 4(k_0^2 \cos^2 \alpha - 2G_1)(k_0^2 \cos^2 \alpha - 2G_2)] \frac{q^4}{4} \\
&\quad + 2G_1 \Omega [\Omega - 2(k_0^2 \cos^2 \alpha - 2G_2)] q^2, \\
b_1 &= 0, \\
b_2 &= -\frac{q^4}{2} - [\Omega + 2(k_0^2 \cos^2 \alpha + G_1 + G_2)] q^2 - \Omega(\Omega + 4G_2).
\end{aligned}$$

## References

1. K. von Klitzing, The quantized Hall effect, *Rev. Mod. Phys.* **58**, 519 (Jul, 1986). doi: 10.1103/RevModPhys.58.519.
2. M. Z. Hasan and C. L. Kane, *Colloquium: Topological insulators*, *Rev. Mod. Phys.* **82**, 3045 (Nov, 2010). doi: 10.1103/RevModPhys.82.3045.
3. X.-L. Qi and S.-C. Zhang, Topological insulators and superconductors, *Rev. Mod. Phys.* **83**, 1057 (Oct, 2011). doi: 10.1103/RevModPhys.83.1057.
4. F. Wilczek, Majorana returns, *Nat. Phys.* **5**, 614 (Sep, 2009). doi: 10.1038/nphys1380.
5. J. D. Koralek, C. P. Weber, J. Orenstein, B. A. Bernevig, S.-C. Zhang, S. Mack, and D. D. Awschalom, Emergence of the persistent spin helix in semiconductor quantum wells, *Nature*. **458**, 610 (Apr, 2009). doi: 10.1038/nature07871.
6. J. Dalibard, F. Gerbier, G. Juzeliūnas, and P. Öhberg, *Colloquium: Artificial gauge potentials for neutral atoms*, *Rev. Mod. Phys.* **83**, 1523 (Nov, 2011). doi: 10.1103/RevModPhys.83.1523.
7. M. V. Berry, Quantal Phase Factors Accompanying Adiabatic Changes, *Proc. R. Soc. A*. **392**(1802), 45 (1984). doi: 10.1098/rspa.1984.0023.
8. J. Ruseckas, G. Juzeliūnas, P. Öhberg, and M. Fleischhauer, Non-Abelian Gauge Potentials for Ultracold Atoms with Degenerate Dark States, *Phys. Rev. Lett.* **95**, 010404 (Jun, 2005). doi: 10.1103/PhysRevLett.95.010404.
9. S.-L. Zhu, H. Fu, C.-J. Wu, S.-C. Zhang, and L.-M. Duan, Spin Hall Effects for Cold Atoms in a Light-Induced Gauge Potential, *Phys. Rev. Lett.* **97**, 240401 (Dec, 2006). doi: 10.1103/PhysRevLett.97.240401.
10. K. J. Günter, M. Cheneau, T. Yefsah, S. P. Rath, and J. Dalibard, Practical scheme for a light-induced gauge field in an atomic Bose gas, *Phys. Rev. A*. **79**, 011604 (Jan, 2009). doi: 10.1103/PhysRevA.79.011604.
11. N. R. Cooper and Z. Hadzibabic, Measuring the Superfluid Fraction of an Ultracold Atomic Gas, *Phys. Rev. Lett.* **104**, 030401 (Jan, 2010). doi: 10.1103/PhysRevLett.104.030401.
12. P. Hauke, O. Tieleman, A. Celi, C. Ölschläger, J. Simonet, J. Struck, M. Weinberg, P. Windpassinger, K. Sengstock, M. Lewenstein, and A. Eckardt, Non-Abelian Gauge Fields and Topological Insulators in Shaken Optical Lattices, *Phys. Rev. Lett.* **109**, 145301 (Oct, 2012). doi: 10.1103/PhysRevLett.109.145301.
13. I. B. Spielman, Raman processes and effective gauge potentials, *Phys. Rev. A*. **79**, 063613 (Jun, 2009). doi: 10.1103/PhysRevA.79.063613.
14. Y.-J. Lin, R. L. Compton, A. R. Perry, W. D. Phillips, J. V. Porto, and I. B. Spielman, Bose-Einstein Condensate in a Uniform Light-Induced Vector Potential, *Phys. Rev. Lett.* **102**, 130401 (Mar, 2009). doi: 10.1103/PhysRevLett.102.130401.
15. Y.-J. Lin, R. L. Compton, K. Jimenez-Garcia, J. V. Porto, and I. B. Spielman, Synthetic magnetic fields for ultracold neutral atoms, *Nature*. **462**, 628 (Dec, 2009). doi: 10.1038/nature08609.
16. J. Struck, C. Ölschläger, R. Le Targat, P. Soltan-Panahi, A. Eckardt,

- M. Lewenstein, P. Windpassinger, and K. Sengstock, Quantum Simulation of Frustrated Classical Magnetism in Triangular Optical Lattices, *Science*. **333**(6045), 996 (2011). doi: 10.1126/science.1207239.
17. C. V. Parker, L.-C. Ha, and C. Chin, Majorana returns, *Nat. Phys.* **9**, 769 (Dec, 2013). doi: 10.1038/nphys2789.
  18. Y.-J. Lin, K. Jimenez-Garcia, and I. B. Spielman, Spin-orbit-coupled Bose-Einstein condensates, *Nature*. **471**, 83 (Mar, 2011). doi: 10.1038/nature09887.
  19. Y. A. Bychkov and E. I. Rashba, Oscillatory effects and the magnetic susceptibility of carriers in inversion layers, *J. Phys. C: Solid State Phys.* **17** (33), 6039 (1984). doi: 0.1088/0022-3719/17/33/015.
  20. G. Dresselhaus, Spin-Orbit Coupling Effects in Zinc Blende Structures, *Phys. Rev.* **100**, 580 (Oct, 1955). doi: 10.1103/PhysRev.100.580.
  21. P. Wang, Z.-Q. Yu, Z. Fu, J. Miao, L. Huang, S. Chai, H. Zhai, and J. Zhang, Spin-Orbit Coupled Degenerate Fermi Gases, *Phys. Rev. Lett.* **109**, 095301 (Aug, 2012). doi: 10.1103/PhysRevLett.109.095301.
  22. L. W. Cheuk, A. T. Sommer, Z. Hadzibabic, T. Yefsah, W. S. Bakr, and M. W. Zwierlein, Spin-Injection Spectroscopy of a Spin-Orbit Coupled Fermi Gas, *Phys. Rev. Lett.* **109**, 095302 (Aug, 2012). doi: 10.1103/PhysRevLett.109.095302.
  23. V. Galitski and I. B. Spielman, Spin-orbit coupling in quantum gases, *Nature*. **494**, 49 (Feb, 2013). doi: 10.1038/nature11841.
  24. N. Goldman, G. Juzeliūnas, P. Öhberg, and I. B. Spielman, Light-induced gauge fields for ultracold atoms, *Rep. Progr. Phys.* **77**(12), 126401 (Nov, 2014). doi: 10.1088/0034-4885/77/12/126401.
  25. H. Zhai, Degenerate quantum gases with spin-orbit coupling: a review, *Rep. Progr. Phys.* **78**(2), 026001 (Feb, 2015). doi: 10.1088/0034-4885/78/2/026001.
  26. W. Zheng, B. Liu, J. Miao, C. Chin, and H. Zhai, Strong Interaction Effects and Criticality of Bosons in Shaken Optical Lattices, *Phys. Rev. Lett.* **113**, 155303 (Oct, 2014). doi: 10.1103/PhysRevLett.113.155303.
  27. Y. Li, L. P. Pitaevskii, and S. Stringari, Quantum Tricriticality and Phase Transitions in Spin-Orbit Coupled Bose-Einstein Condensates, *Phys. Rev. Lett.* **108**, 225301 (May, 2012). doi: 10.1103/PhysRevLett.108.225301.
  28. M. Boninsegni and N. V. Prokof'ev, *Colloquium: Supersolids: What and where are they?*, *Rev. Mod. Phys.* **84**, 759 (May, 2012). doi: 10.1103/RevModPhys.84.759.
  29. T.-L. Ho and S. Zhang, Bose-Einstein Condensates with Spin-Orbit Interaction, *Phys. Rev. Lett.* **107**, 150403 (Oct, 2011). doi: 10.1103/PhysRevLett.107.150403.
  30. Y. Li, G. I. Martone, and S. Stringari, Sum rules, dipole oscillation and spin polarizability of a spin-orbit coupled quantum gas, *EPL*. **99**(5), 56008 (2012).
  31. L. D. Landau and E. M. Lifshitz, *Statistical Physics, Part 1*, 3rd edn. Oxford, Pergamon (1980).
  32. J.-Y. Zhang, S.-C. Ji, Z. Chen, L. Zhang, Z.-D. Du, B. Yan, G.-S. Pan, B. Zhao, Y.-J. Deng, H. Zhai, S. Chen, and J.-W. Pan, Collective Dipole

- Oscillations of a Spin-Orbit Coupled Bose–Einstein Condensate, *Phys. Rev. Lett.* **109**, 115301 (Sep, 2012). doi: 10.1103/PhysRevLett.109.115301.
33. W. Zheng and Z. Li, Collective modes of a spin-orbit-coupled Bose–Einstein condensate: A hydrodynamic approach, *Phys. Rev. A* **85**, 053607 (May, 2012). doi: 10.1103/PhysRevA.85.053607.
  34. G. I. Martone, Y. Li, L. P. Pitaevskii, and S. Stringari, Anisotropic dynamics of a spin-orbit-coupled Bose–Einstein condensate, *Phys. Rev. A* **86**, 063621 (Dec, 2012). doi: 10.1103/PhysRevA.86.063621.
  35. Y. Li, G. I. Martone, L. P. Pitaevskii, and S. Stringari, Superstripes and the Excitation Spectrum of a Spin-Orbit-Coupled Bose–Einstein Condensate, *Phys. Rev. Lett.* **110**, 235302 (Jun, 2013). doi: 10.1103/PhysRevLett.110.235302.
  36. L. Santos, G. V. Shlyapnikov, and M. Lewenstein, Roton-Maxon Spectrum and Stability of Trapped Dipolar Bose–Einstein Condensates, *Phys. Rev. Lett.* **90**, 250403 (Jun, 2003). doi: 10.1103/PhysRevLett.90.250403.
  37. T. Macrì, F. Maucher, F. Cinti, and T. Pohl, Elementary excitations of ultracold soft-core bosons across the superfluid-supersolid phase transition, *Phys. Rev. A* **87**, 061602 (Jun, 2013). doi: 10.1103/PhysRevA.87.061602.
  38. S. Saccani, S. Moroni, and M. Boninsegni, Excitation Spectrum of a Supersolid, *Phys. Rev. Lett.* **108**, 175301 (Apr, 2012). doi: 10.1103/PhysRevLett.108.175301.
  39. S.-C. Ji, L. Zhang, X.-T. Xu, Z. Wu, Y. Deng, S. Chen, and J.-W. Pan, Softening of Roton and Phonon Modes in a Bose–Einstein Condensate with Spin-Orbit Coupling, *Phys. Rev. Lett.* **114**, 105301 (Mar, 2015). doi: 10.1103/PhysRevLett.114.105301.
  40. M. A. Khamsehchi, Y. Zhang, C. Hamner, T. Busch, and P. Engels, Measurement of collective excitations in a spin-orbit-coupled Bose–Einstein condensate, *Phys. Rev. A* **90**, 063624 (Dec, 2014). doi: 10.1103/PhysRevA.90.063624.
  41. L.-C. Ha, L. W. Clark, C. V. Parker, B. M. Anderson, and C. Chin, Roton-Maxon Excitation Spectrum of Bose Condensates in a Shaken Optical Lattice, *Phys. Rev. Lett.* **114**, 055301 (Feb, 2015). doi: 10.1103/PhysRevLett.114.055301.
  42. L. P. Pitaevskii and S. Stringari, *Bose–Einstein Condensation*. Oxford University Press, New York (2003).
  43. M. Klawunn, A. Recati, L. P. Pitaevskii, and S. Stringari, Local atom-number fluctuations in quantum gases at finite temperature, *Phys. Rev. A* **84**, 033612 (Sep, 2011). doi: 10.1103/PhysRevA.84.033612.
  44. S. Hoinka, M. Lingham, M. Delehay, and C. J. Vale, Dynamic Spin Response of a Strongly Interacting Fermi Gas, *Phys. Rev. Lett.* **109**, 050403 (Aug, 2012). doi: 10.1103/PhysRevLett.109.050403.
  45. L. P. Pitaevskii and S. Stringari, Uncertainty principle, quantum fluctuations, and broken symmetries, *J. Low Temp. Phys.* **85**(5-6), 377 (1991). ISSN 0022-2291. doi: 10.1007/BF00682193.
  46. L. P. Pitaevskii and S. Stringari, Uncertainty principle and off-diagonal long-range order in the fractional quantum Hall effect, *Phys. Rev. B* **47**, 10915

- (Apr, 1993). doi: 10.1103/PhysRevB.47.10915.
47. D. M. Stamper-Kurn, H.-J. Miesner, S. Inouye, M. R. Andrews, and W. Ketterle, Collisionless and Hydrodynamic Excitations of a Bose-Einstein Condensate, *Phys. Rev. Lett.* **81**, 500 (Jul, 1998). doi: 10.1103/PhysRevLett.81.500.
  48. T. Ozawa, L. P. Pitaevskii, and S. Stringari, Supercurrent and dynamical instability of spin-orbit-coupled ultracold Bose gases, *Phys. Rev. A* **87**, 063610 (Jun, 2013). doi: 10.1103/PhysRevA.87.063610.
  49. C. Wang, C. Gao, C.-M. Jian, and H. Zhai, Spin-Orbit Coupled Spinor Bose-Einstein Condensates, *Phys. Rev. Lett.* **105**, 160403 (Oct, 2010). doi: 10.1103/PhysRevLett.105.160403.
  50. C.-J. Wu, I. Mondragon-Shem, and X.-F. Zhou, Unconventional Bose-Einstein Condensations from Spin-Orbit Coupling, *Chin. Phys. Lett.* **28**(9), 97102 (2011). doi: 10.1088/0256-307X/28/9/097102.
  51. S. Sinha, R. Nath, and L. Santos, Trapped Two-Dimensional Condensates with Synthetic Spin-Orbit Coupling, *Phys. Rev. Lett.* **107**, 270401 (Dec, 2011). doi: 10.1103/PhysRevLett.107.270401.
  52. T. Ozawa and G. Baym, Striped states in weakly trapped ultracold Bose gases with Rashba spin-orbit coupling, *Phys. Rev. A* **85**, 063623 (Jun, 2012). doi: 10.1103/PhysRevA.85.063623.
  53. D. A. Zezyulin, R. Driben, V. V. Konotop, and B. A. Malomed, Nonlinear modes in binary bosonic condensates with pseudo-spin-orbital coupling, *Phys. Rev. A* **88**, 013607 (Jul, 2013). doi: 10.1103/PhysRevA.88.013607.
  54. Z. Lan and P. Öhberg, Raman-dressed spin-1 spin-orbit-coupled quantum gas, *Phys. Rev. A* **89**, 023630 (Feb, 2014). doi: 10.1103/PhysRevA.89.023630.
  55. Q. Sun, L. Wen, W.-M. Liu, G. Juzeliūnas, and A.-C. Ji, Tunneling-assisted spin-orbit coupling in bilayer Bose-Einstein condensates, *Phys. Rev. A* **91**, 033619 (Mar, 2015). doi: 10.1103/PhysRevA.91.033619.
  56. W. Han, G. Juzeliūnas, W. Zhang, and W.-M. Liu, Supersolid with nontrivial topological spin textures in spin-orbit-coupled Bose gases, *Phys. Rev. A* **91**, 013607 (Jan, 2015). doi: 10.1103/PhysRevA.91.013607.
  57. C. Hickey and A. Paramekanti, Thermal Phase Transitions of Strongly Correlated Bosons with Spin-Orbit Coupling, *Phys. Rev. Lett.* **113**, 265302 (Dec, 2014). doi: 10.1103/PhysRevLett.113.265302.
  58. A. F. Andreev and I. M. Lifshitz, Quantum Theory of Defects in Crystals, *JETP* **29**, 1107 (1969).
  59. A. J. Leggett, Can a Solid Be “Superfluid”?, *Phys. Rev. Lett.* **25**, 1543 (Nov, 1970). doi: 10.1103/PhysRevLett.25.1543.
  60. G. V. Chester, Speculations on Bose-Einstein Condensation and Quantum Crystals, *Phys. Rev. A* **2**, 256 (Jul, 1970). doi: 10.1103/PhysRevA.2.256.
  61. M. Kunimi and Y. Kato, Mean-field and stability analyses of two-dimensional flowing soft-core bosons modeling a supersolid, *Phys. Rev. B* **86**, 060510 (Aug, 2012). doi: 10.1103/PhysRevB.86.060510.
  62. C. J. Pethick and H. Smith, *Bose-Einstein Condensation in Dilute Gases*, 2 edn. Cambridge University Press, New York (2003).

63. R. Barnett, S. Powell, T. Graß, M. Lewenstein, and S. Das Sarma, Order by disorder in spin-orbit-coupled Bose–Einstein condensates, *Phys. Rev. A*, **85**, 023615 (Feb, 2012). doi: 10.1103/PhysRevA.85.023615.
64. X.-Q. Xu and J. H. Han, Emergence of Chiral Magnetism in Spinor Bose–Einstein Condensates with Rashba Coupling, *Phys. Rev. Lett.* **108**, 185301 (Apr, 2012). doi: 10.1103/PhysRevLett.108.185301.
65. R. Liao, Z.-G. Huang, X.-M. Lin, and W.-M. Liu, Ground-state properties of spin-orbit-coupled Bose gases for arbitrary interactions, *Phys. Rev. A*, **87**, 043605 (Apr, 2013). doi: 10.1103/PhysRevA.87.043605.
66. N. N. Bogoliubov, Quasimittelwerte in Problemen der statistischen Mechanik, *Phys. Abh. SU*, **6**, 1 (1962).
67. G. I. Martone, Y. Li, and S. Stringari, Approach for making visible and stable stripes in a spin-orbit-coupled Bose–Einstein superfluid, *Phys. Rev. A*, **90**, 041604 (Oct, 2014). doi: 10.1103/PhysRevA.90.041604.
68. G. I. Martone, Visibility and stability of superstripes in a spin-orbit-coupled Bose–Einstein condensate, *Eur. Phys. J. Special Topics*, **224**(3), 553 (Apr, 2015). doi: 10.1140/epjst/e2015-02386-x.